INTERNATIONAL JOURNAL FOR NUMERICAL METHODS IN FLUIDS
Int. J. Numer. Meth. Fluids 2008; **58**:319–353
DOI: 10.1002/fld.1728

DEM prediction of particle flows in grinding processes

P. W. Cleary[1,*,†], M. D. Sinnott[1] and R. D. Morrison[2]

[1]*CSIRO Mathematical and Information Sciences, Private Bag 33, Clayton, Vic. 3168, Australia*
[2]*Julius Kruttschnitt Mineral Research Center, The University of Queensland, Isles Rd, Indooroopilly, Qld. 4068, Australia*

SUMMARY

Particle size reduction is a critical unit process in many industries including mineral processing, cement, food processing, pigments and industrial minerals and pharmaceuticals. The aim is to take large feed material and as efficiently as possible reduce the size of the particles to a target size range. Over time, a very large range of equipment has been developed to perform this for many materials and in many different conditions. Discrete element method (DEM) modelling is a computational tool that can allow detailed exploration of the particle flow and breakage processes within comminution equipment and can assist in developing a clearer and more comprehensive understanding of the detailed processes occurring within. In this paper, we examine the particle and energy flows in representative examples of the equipment used in many grinding processes. We study a 36′ semi-autogenous mill used in primary grinding for mineral processing, a ball mill used for cement clinker grinding, a grinding table also used for cement grinding, a tower mill used for fine grinding both in mineral processing and for industrial minerals and finally for an Isamill, which is used for ultra-fine grinding in mineral processing. Copyright © 2008 John Wiley & Sons, Ltd.

Received 22 March 2007; Revised 12 November 2007; Accepted 20 November 2007

KEY WORDS: comminution; milling; particles; breakage; energy utilization; DEM

1. INTRODUCTION

Particle breakage is an essential process in many different industries, ranging from mineral processing, quarrying, cement to food processing and pharmaceuticals. The aim is to reduce the original feed stock particles from the sizes supplied to the much smaller sizes required for either further processing or to be a part of final products. In some industries, particularly mineral

---

[*] Correspondence to: P. W. Cleary, CSIRO Mathematical and Information Sciences, Private Bag 33, Clayton, Vic. 3168, Australia.

[†] E-mail: paul.cleary@csiro.au

processing, the intent is to do this as efficiently as possible (that is, with respect to energy consumption and wear materials), producing optimal sizes for liberating target minerals at maximum mill throughput and minimizing operating costs. For a good introduction to the issues of comminution in mineral processing, see [1]. In industries such as food and pharmaceuticals, the mill sizes are much smaller and capital and energy costs are unimportant, but the final product specifications are tight and the focus is on quality and cleanliness/avoidance of contamination.

Size reduction is typically accomplished in a series of stages whose design is highly dependent on the nature and size of the feed stock and the reduction ratio that is required. The first stage in mining and mineral processing is usually some form of blasting to liberate ore and waste from the deposit. A typical mineral processing grinding circuit is tailored to the properties of the particular mine ore. Commonly, this involves two or more classes of equipment starting with crushers, followed by semi-autogenous (SAG) mills and then sometimes ball mills. Occasionally, high-pressure grinding rolls or other novel devices are substituted. For cement industries, multi-stage ball mills, roller mills or grinding tables and high-pressure grinding rolls are often used, sometimes in series. For fine and ultra-fine grinding, particles will typically pass through a number of stages of grinding, finishing with tower mills or stirred mills such as the Netzsch or Isamill.

Regardless of the industry and which of the possible outcomes is required, the size reduction process needs to be better understood and optimized for those applications. Traditionally, this has been done using extensive laboratory, pilot scale and field trials. These are expensive and time consuming and allow models to be constructed that are limited by the range of conditions tested and the complexities of the many different processes occurring within these mills. For a good introduction to data fitted modelling of a broad range of comminution equipment, see [1]. Traditional experimental and modelling approaches are not well placed to create the required insights into comminution fundamentals or facilitate radical step changes in performance. Computational modelling, using the discrete element method (DEM), has been growing in capability over the past decade and is now able to provide significant insights into the operation of existing and future mills and can be used as a tool to aid equipment and process design and optimization.

DEM has been used for modelling a wide range of industrial applications, particularly in milling. Early work on ball mills by Mishra and Rajamani [2, 3] has been followed by Cleary [4, 5] and Cleary and Sawley [6]. Axial transport and grate discharge were studied in [7]. Similarly, SAG mills were modelled by Rajamani and Mishra [8] and subsequently by others [9–12]. Experimental validation has been performed for a centrifugal mill [13] and for charge motion and shape in a laboratory scale model SAG mill [14–16] and for grinding rates [17]. Other applications include vibrational segregation [18–20], flows in rotating drums [19–21], hopper flows by Ristow [19] Potapov and Campbell [22] and many more. A broad range of applications simulated using DEM by Cleary *et al.* are reviewed in [23].

2. DISCRETE ELEMENT METHOD

DEM is a simulation method that models particulate systems whose motions are dominated by collisions. This involves following the motion of every particle or object in the flow and modelling each collision between the particles and between the particles and their environment (stationary and moving objects such as mills and crushers). The discrete element algorithm has three main stages:

1. A search grid is used to periodically build a near-neighbour interaction list that contains all the particle pairs and object–particle pairs that are likely to experience collisions in the short term. Using only pairs in this list reduces the force calculation to an $O(M)$ operation, where M is the total number of particles. Industrial simulations with 2 million particles are now possible in reasonable times on current single-processor workstations.
2. The forces on each pair of colliding particles and/or boundary objects are evaluated in their local reference frame using a suitable contact force model and then transformed into the simulation frame of reference.
3. All the forces and torques on each particle and object are summed and the resulting equations of motion are integrated to give the resulting motion of these bodies. Time integration is performed using a second-order predictor–corrector scheme and typically uses between 15 and 25 time steps to accurately integrate each collision. This leads to small time steps (typically 10^{-4}–10^{-6} s depending on the controlling length and time scales for each application).

2.1. Collision model

The general DEM methodology and its variants are well established and are described in review articles [24–26]. The implementation used here is described in more detail in Cleary [4, 20, 23]. Briefly, the particles are allowed to overlap and the amount of overlap Δx, and normal v_{n} and tangential v_{t} relative velocities determine the collisional forces via a contact force law. There are a number of possible contact force models available in the literature that approximate collision dynamics to various extents. We use a linear spring-dashpot model that is shown diagrammatically in Figure 1. For more complex models, see [26, 27].

The normal force

$$F_{\text{n}} = -k_{\text{n}}\Delta x + C_{\text{n}}v_{\text{n}} \tag{1}$$

consists of a linear spring to provide the repulsive force and a dashpot to dissipate a proportion of the relative kinetic energy. The maximum overlap between particles is determined by the stiffness k_{n} of the spring in the normal direction. Typically, average overlaps of 0.1–0.5% of the particle diameter are desirable, requiring spring constants of the order of 10^6–10^8 N/m in three dimensions.

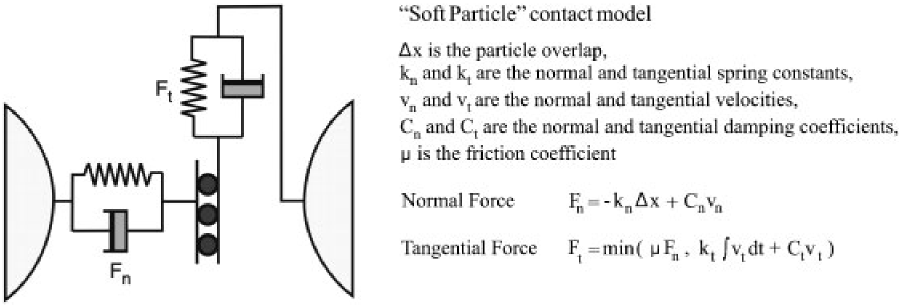

"Soft Particle" contact model

Δx is the particle overlap,
k_n and k_t are the normal and tangential spring constants,
v_n and v_t are the normal and tangential velocities,
C_n and C_t are the normal and tangential damping coefficients,
μ is the friction coefficient

Normal Force $F_n = -k_n \Delta x + C_n v_n$

Tangential Force $F_t = \min(\mu F_n,\ k_t \int v_t\,dt + C_t v_t)$

Figure 1. Contact force law consisting of springs, dashpots and frictional sliders used for evaluating forces between interacting particles and boundaries.

The normal damping coefficient C_n is chosen to give the required coefficient of restitution ε (defined as the ratio of the post-collisional to pre-collisional normal component of the relative velocity), and is given in [20].

The tangential force is given by

$$F_t = \min\left\{\mu F_n, k_t \int v_t \, dt + C_t v_t\right\} \tag{2}$$

where the vector force F_t and velocity v_t are defined in the plane tangent to the surface at the contact point. The integral term represents an incremental spring that stores energy from the relative tangential motion and models the elastic tangential deformation of the contacting surfaces, while the dashpot dissipates energy from the tangential motion and models the tangential plastic deformation of the contact. Depending on the history of the contact, it is possible for the spring to be loading in one direction and simultaneously unloading in the orthogonal direction. The total tangential force F_t is limited by the Coulomb frictional limit μF_n, at which point the surface contact shears and the particles begin to slide over each other.

2.2. *Geometry representation*

Industrial applications place heavy demands on the geometric capabilities of DEM codes, particularly for three-dimensional geometries. In our DEM code, any two-dimensional cross section can be constructed using an appropriate number of line segments, circular segments or discs. This gives essentially unrestricted geometric capability. In three dimensions, boundary objects are constructed by either extruding two-dimensional cross sections or using triangular finite-element style surface meshes. Such meshes can be produced using any reasonable mesh generator from solid models generated in most CAD packages. This provides enormous flexibility in specifying three-dimensional environments with which the particles interact.

2.3. *Particle shape*

The particles are represented either as spheres or super-quadrics, which in a standard frame of reference are given by

$$\left(\frac{x}{a}\right)^m + \left(\frac{y}{b}\right)^m + \left(\frac{z}{c}\right)^m = 1 \tag{3}$$

The ratios of the semi-major axes b/a and c/a are the aspect ratios of the particles and the super-quadric power m determines the shape of the particle. For $m=2$ elliptical particles are obtained. If additionally $a=b=c$, then the particles are spherical. As m increases, the shape becomes progressively more cubic, with the corners becoming sharper and the particle more blocky. By $m=10$, the particle shape is essentially a cube (for aspect ratios 1). This is a very flexible class of shapes, which varies continuously (m is not restricted to integer values). This allows plausible shape distributions to be represented and the shape can be made to change dynamically during simulation (for example, with abrasion as measured by the shear energy dissipation on the particle). The computational cost of simulations using super-quadrics is currently between 2 and 5 times that of using spheres. This shape description was introduced to DEM in two dimensions in [28] and in three dimensions in [23].

2.4. Model outputs

The nature of the quantitative predictions that one wants to make, using the extensive state data available in DEM simulations, depends very much on the application and the questions one is seeking to answer. For industrial applications we typically calculate:

- Boundary stresses (for mechanical design and fatigue prediction, including coupling to FEM for structure response prediction).
- Wear rates and distributions (for estimating the lifespan of equipment and wear components).
- Accretion rates (for predicting accretion-induced blockage, changes in open area of screens).
- Collisional force distributions, collision frequencies, energy absorption spectra (for understanding breakage and agglomeration).
- Power consumption and torques (for equipment design).
- Flow rates and flow statistics (for summarizing characteristics of complex flows).
- Sampling statistics (to assess the accuracy of various sampling processes).
- Mixing and segregation rates (to assess the progress of intended mixing and de-mixing processes and to understand the degree of segregation and its effects on other processes where segregation and/or mixing are not intended).
- Residence time distributions (to assess the range of times that particles are exposed to various environments within a process, for example in granulation and in comminution).
- Axial transport rates (to assess the axial flow along cylinders (rotating and stationary) that are commonly used).

For more details on the simulation method and on the data analysis see Cleary [20, 23].

3. TUMBLING MILLS

Tumbling mills are large cylindrical vessels that rotate about their axes at reasonable fractions of the speed required to centrifuge the particulate material that is ground within. The grinding is produced by a range of mechanisms including high-speed impact, abrasion, chipping and nipping of small particles between large ones. Grinding is often augmented by adding various types of grinding media. There are several specific variants of the tumbling mill, which are distinguished by their size, the size of material fed to the mill and the type of grinding media. These include:

- Autogenous grinding (AG) mills, which are fed a mixture of large and small rocks with the large rocks acting as grinding media.
- SAG mills are the largest tumbling mills used (up to 40′ or 12.2 m diameter) and are used for primary grinding, mainly in mineral processing, using a coarse feed (typically up to 250 mm diameter rock) coming from some arrangement of crushers. There is insufficient coarse rock to produce large impacts so the charge is augmented by steel grinding balls. These can make up between 30 and 50% of the volume of the charge. However, neither large rocks nor balls produce very many large impacts as discussed later.
- Rod mills are mills where the grinding media consist of large rods (often almost the length of the mill). These mills typically take a relatively fine feed material of perhaps 20 mm topsize, (see [23] for an example of DEM modelling of a rod mill).
- Ball mills are typically used for secondary grinding in mineral processing, taking feed from a SAG mill or an equivalent device. It is typically smaller than the SAG mill (3–8 m diameter)

DOI: 10.1002/fld

and has higher ball loadings using smaller balls and with a finer feed. Ball mills are also commonly used in cement clinker grinding. These mills tend to be at the smaller end of the size range and have less aggressively designed lifters.

In this paper, we present results for a large-scale model of a 36′ (10.86 m) diameter SAG mill used in mineral processing and for a 4 m diameter (first compartment) ball mill used for cement grinding for coarse and fine feeds.

3.1. SAG mill

The SAG mill used in this modelling is a common design 36′ or 10.86 m diameter SAG mill, which would typically be used for hard rock mineral processing. This mill rotates at 10 rpm (which is 78% of the critical speed at which the particles within the mill will centrifuge). Since collisions of the rock with the mill wear the mill surface, the mill is lined with a replaceable liner, typically made of high-grade collision- and abrasion-resistant steel. The liner serves a dual purpose of protecting the expensive mill shell and gearing from damage, and locking into the charge to lift it higher and deliver more energy into the charge to increase the rate of grinding.

Here, we use a traditional 72 row (typically twice the diameter of the mill measured in feet) configuration of symmetric, close packed, steep face angle lifters (7°). The overall fill level of the charge is 30% of the mill volume. The ball loading is 10% (of the mill volume) or around $\frac{1}{3}$ of the charge (by volume). The ball size distribution is given in Table I. A typical rock size distribution for a hard rock ore is also used and this is also given in Table I. The top size of the balls used is 125 mm and the top size of the rock is 200 mm. The rocks are correctly resolved down to 6 mm with smaller rocks neglected.

Previously [14] we have established, by detailed comparison of various DEM models with experiments for a scale model SAG mill, that two-dimensional models have significant quantitative errors. Therefore, we need to use some form of three-dimensional model. Since the mill geometry is symmetric along its length, we are able to model the charge motion in a 0.5 m wide axial slice of mill. A key difference between a three-dimensional slice model and a two-dimensional model is that the particles are represented as spheres rather than as cylinders and lock together in three-dimensional particle structures that are stronger than the simpler structures possible in two dimensions. Hence, although the overall charge shape is invariant in the axial direction, the

Table I. Rock and ball size distributions for a 1.2 million particle SAG mill model.

Balls		Rocks	
−125 to +88 mm	30%	−200 to +140 mm	8%
−88 to +63 mm	40%	−140 to +100 mm	12%
−63 to +44 mm	20%	−100 to +70 mm	15%
−44 to +31 mm	10%	−70 to +50 mm	15%
		−50 to +35 mm	15%
		−35 to +25 mm	10%
		−25 to +18 mm	10%
		−18 to +12.5 mm	10%
		−12.5 to +8.5 mm	4%
		−8.5 to +6 mm	1%

three-dimensional particle interactions are important to predicting the correct flow dynamics. A second key need for using a three-dimensional model is that the energy transfer mechanisms during collision depend on the masses of the interacting particles. In two dimensions, the cylindrical particle masses vary as the square of the radius, whereas in three dimensions they vary as the cube. Hence, to obtain meaningful collision energy spectra from which we make deductions about comminution performance, it is essential to perform the simulations in three-dimensions. This 0.5 m slice is sufficiently wide to properly represent particle motion in a long mill. This type of model is therefore suitable for predicting breakage, power consumption, belly-lifter wear and to understand the main flow patterns of the charge. If one were interested in axial transport then the full length of the mill needs to be modelled [7]. The current SAG configuration was previously modelled [10, 12] using a similar rock size distribution but with the rock size truncated at a much higher size of 25 mm. In this paper, we present simulation predictions using the more realistic 6 mm cut-off for the rock size distribution. This involves simulating 1.2 million particles in this system.

Figure 2 shows the charge distribution looking along the axis of the SAG mill. The charge surface has a very clear bi-linear shape, rising slowly from the toe to the middle of the charge and then steeply up to the shoulder. Substantial cataracting streams depart from the lifters above the shoulder and fall in well-defined coherent bands to impact on the liner above the toe at around the 3 O’clock position. There is a central slow-moving band within the charge midway between the free surface and the mill liner with strong shear on either side. The cataracting stream reaches around 7 m/s as it hits the liner above the toe of the charge.

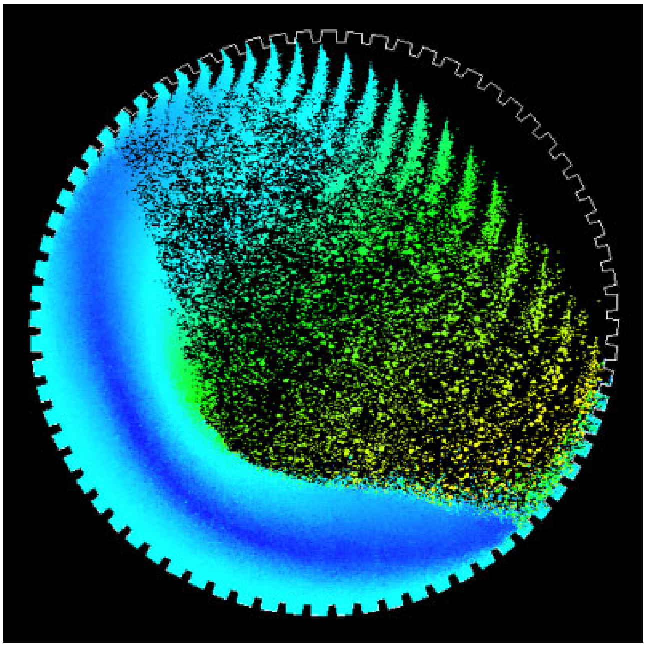

Figure 2. Slice model of a 36′ SAG mill with 1.2 million particles coloured by speed with red being 19 m/s and dark blue being stationary.

DOI: 10.1002/fld

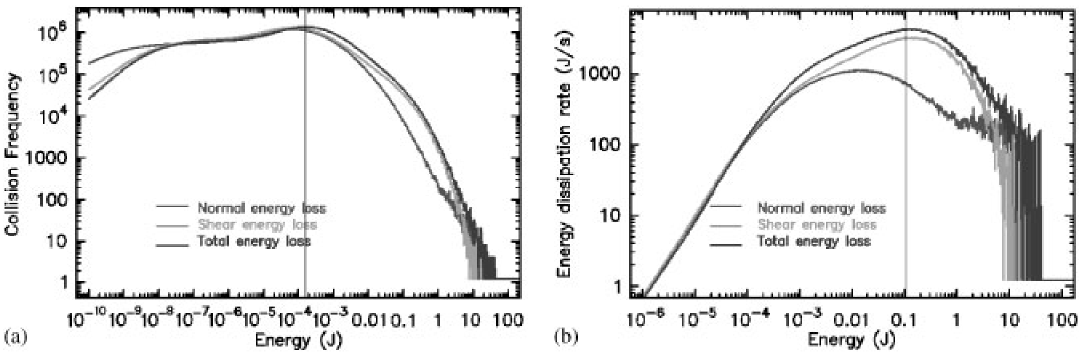

Figure 3. Energy spectra for 36′ SAG mill: (a) frequency distribution of different collision energies and (b) rate of energy dissipation at each collision energy.

The power prediction for this 0.5 m axial slice of the mill is 796 kW. This is very close to the average power draw reported in Cleary [10] of 778 kW for the case with a 25 mm cut-off for the rock size. This suggests that the lower cut-off has little effect on the power draw prediction. For the full 6 m axial length of the mill we would therefore expect a power draw of 9.54 MW.

Figure 3 shows the way in which the energy consumed by the mill is dissipated. The left plot shows the frequency distribution of the various collision energies. The peak energies, corresponding to the largest rocks and balls falling at the top of the cataracting stream, are 50 J. However, in comparison with the numbers of rocks, there are very few of these high-energy impacts. The most common collisions occur for very low energies around 0.1 mJ with frequencies exceeding 1 million collisions per second. There are enormous numbers of collisions recorded at even lower energies (down to the minimum of 10^{-10} J). Of more interest is the energy dissipated at each of these energy levels. This is shown in the right plot and indicates that energy levels of around 100 W are being dissipated by the highest energy collisions. The strongest energy dissipation rate occurs at around 0.15 J with around 5 kW dissipated by these collisions. The energy dissipated per energy level decreases slowly until around 0.1 mJ and then drops linearly and more rapidly, so that by the 10^{-6} J level only 1 W of energy is being dissipated, despite there being a frequency of a million collisions per second. Hence, although there are enormous numbers of collisions at these small energy levels, the total energy dissipated by these very gentle collisions is minimal.

Comparing the distributions of shear and normal collision energies in Figure 3, it is clear that the shear energy levels are consistently higher than the normal ones. The shear energy dissipation rate (shown in the lower plot of Figure 3) occurs at 0.2 J, which is double that of the overall maximum dissipation rate and 20 times higher than the energy level for the maximum normal energy dissipation rate (at 0.01 J). The area between the shear and normal energy curves is the difference in the total energy consumption for impact and abrasion collision modes. Remembering that the vertical scale is logarithmic, the difference between these curves is significant. This demonstrates that a large majority of energy dissipation in a SAG mill occurs by particles sliding over and past each other and not by direct head-on impact of the particles.

An alternative approach to the spectra is to consider energy levels by 'tracking' some selected particles in each size class. This approach has demonstrated that breakage in a single impact is highly unlikely for most particles larger than a few millimeters [12]. Hence, a detailed

Table II. Energy usage within the SAG mill.

Collision type	% Total energy in this type
Rock–rock	51.9
Rock–liner	1.2
Rock–media	38.3
Media–media	8.3
Media–liner	0.3

investigation into incremental breakage was carried out. This work found a reasonably well-defined minimum energy below which essentially no impact damage occurs. For impacts with larger energy, the particle accumulates incremental damage, increasing the probability of breakage with each event [29].

Table II shows the distribution of energy dissipation by the different types of collisions occurring in the mill. Around 52% of the energy is dissipated in rock–rock collisions with another 38% dissipated in rock–media collisions (leading to both rock comminution and ball wear). A further 8.3% of the energy is dissipated in ball–ball collisions with some fraction of this leading to ball wear. Only 1.2% of the energy is lost in rock–liner collisions, with some fraction of this contributing to liner wear. A further 0.3% of the energy dissipated is in media–liner collisions and contributes to ball and liner wear. DEM can be used to explore modifications to liner geometry, mill operating parameters, feed and ball size distributions to help move energy dissipation from non-useful categories (such as liner collisions) to rock–rock and rock–media collisions, which should improve grinding rates for the mill.

3.2. Ball mills for cement grinding

Ball mills are often used for grinding clinker as part of the cement production process. Often two chamber mills are used with the chambers separated by a grate. Typically, finer ball charges are used in the second compartment to give a finer grind than is possible in the coarser first compartment. Here we simulate the first compartment configuration of such a ball mill. The liners used for cement mills tend to be less aggressive than those used in mineral processing. Here we use a common wave liner in a mill with an internal shell diameter of 4.0 m. The liner consists of 36 liner plates, each with a plate length of 340 mm and a height of 65 mm, with a single wave per plate. The overall fill level used is 35% (of the volume of the mill) with the charge consisting of half balls and half clinker. The ball size distribution is uniformly mass weighted with a smallest size 50 mm (2 in) and a top size of 95 mm ($3\frac{3}{4}$ in). Two different clinker sizes are used:

- a coarse feed with particles in the range 25–80 mm and
- a fine feed with particles in the range 10–50 mm.

The fine feed case is more typical of cement clinker grinding.

A periodic slice of the mill is again sufficient to predict the dynamics of interest. The periodic slice length used was 250 mm. The mill rotation rate was 16.28 rpm, which is 76% of critical speed (based on a diameter of 3.9 m corresponding to the lowest point in the wave liner). For the coarse feed, the spring stiffness used was 1.5×10^{7} N/m and for the fine feed a value of 2.0×10^{7} N/m was required to give the desired average particle overlaps of 0.5–0.7%. The friction coefficient was 0.5 for all materials. The coefficient of restitution was chosen to be 0.8 for steel–steel collisions, 0.5

DOI: 10.1002/fld

for steel–clinker and 0.3 for clinker–clinker collisions. The number of particles was 11 200 for the coarse charge and 75 000 for the fine charge. The speed of a DEM code can be quantified using the Cundall number (Cu), which is the number of particle time steps per cpu second. On a single processor 3 GHz Pentium, these ball mill simulations produce Cundall numbers of 450 000.

Figure 4 shows the charge distribution in the ball mill for the coarse and fine size feeds. The charge shape is very similar in both cases with the familiar bi-linear shape for the free surface rising from the toe to the inflexion point near the centre of the mill and then steeply up to the shoulder position. Despite the difference in mill size and the size differences in the charge, this flow pattern is fairly similar to that of the SAG mill, but with the inflexion point now closer to the mill axis and the angular difference between the two surfaces of the charge being less severe. It is mainly in the energies delivered to the particles that the mills' behaviour differs. For both

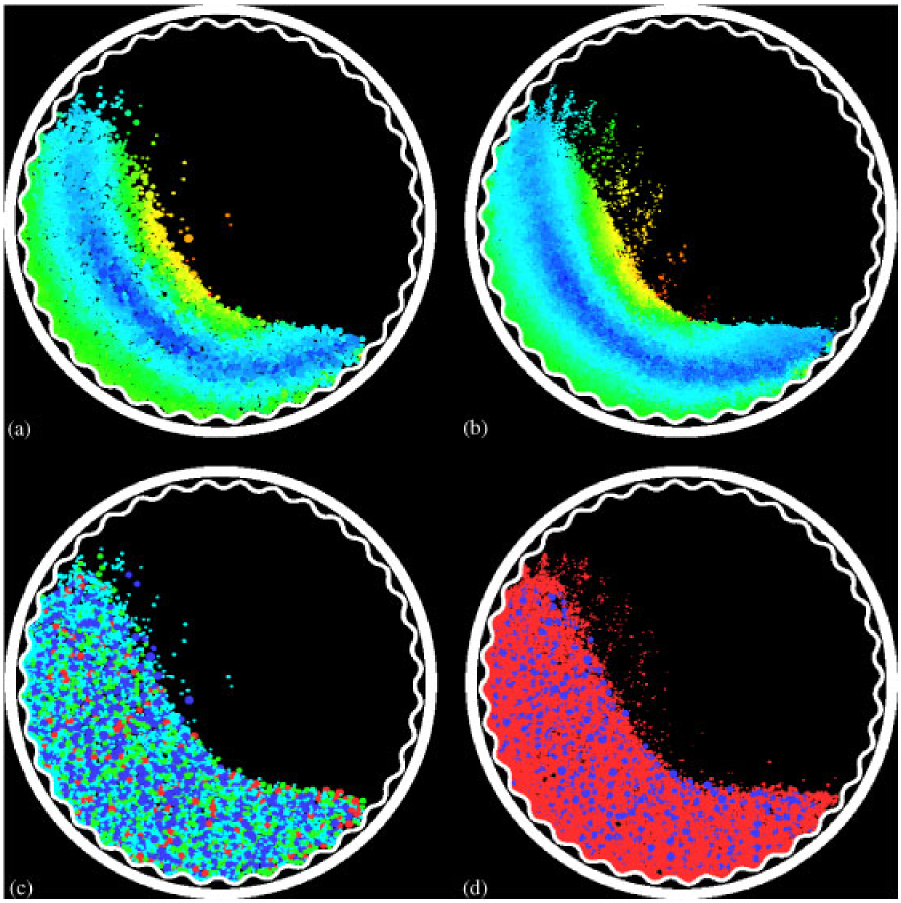

Figure 4. Charge distribution in the ball mill with (left) coarse size distribution and (right) fine size distribution. The top row is coloured by the particle speed (with red being 7 m/s and dark blue being stationary) and the bottom row is coloured by particle class (with dark blue showing the balls).

DOI: 10.1002/fld

coarse and fine feeds, the shoulder position lies in the range of 210–220°, as measured clockwise from the 3 O'clock position. This range reflects the difference in the timing of the disengagement of the charge from different points on the wave lifter. For the high point of the lifter, which is closer to the centre of the mill, the disengagement occurs a little earlier at around 210°, but for the more distant low point of the line, the disengagement occurs around 220°. The toe position for the coarse feed lies in the range of -35 to $-40°$, whereas for the fine feed the toe lies consistently in the tighter range of -35 to $-36°$. The finer feed is more able to cushion the large balls and this damps fluctuations in the avalanching flow, leading to lower variability of the stopping position at the toe. The other visible effect of the finer feed is that the modest cataracting stream is more clearly defined because of the much larger numbers of much smaller particles in this region. The peak particle speeds are consistently around 6.5–7.0 m/s at the bottom of the cataracting stream. The pictures in the lower row of Figure 4 show the particles coloured by their type. The dark blue particles are the balls and they are fairly uniformly distributed throughout the charge. With such a large ball load, it is difficult for the balls to concentrate around the centre of recirculation due to size segregation driven by the centrifugal force (as sometimes occurs for SAG mills).

The power draw predicted for the coarse feed is 146.9 kW/m of mill length or 1.028 MW for a 7 m long ball mill. This corresponds to a torque of 86.2 kN/m average torque (averaged over 6 s of operation of the mill after steady state has been achieved). For the fine feed, the power draw rises slightly to 148.2 kW/m of mill length, corresponding to an average torque of 87.0 kN/m. This represents a 0.9% increase when moving to the finer feed. We attribute this very minor change to the fact that the finer particles are slightly better able to pack the voids between the balls and this will lead to a slightly higher bulk density for the charge whose centre of mass will therefore move slightly closer to the mill shell, thereby increasing the mill power draw. This is a real but weak effect and will continue as the feed is made finer or finer product particles are included in the simulation.

Figure 5 shows the selected energy spectra for the different types of collisions for both feed size distributions. The energy dissipated in every collision is tracked and the frequency distribution of the different collision energy intensities is calculated. This is done for the normal work (as a measure of impact breakage), shear work (as a measure of abrasion/attrition damage) and total work (measuring overall breakage). A variant of the spectra that we use here involves multiplying the energy of collisions by the frequency to give the energy dissipation rate for each collision energy level in the mill. This helps us understand where the 147 kW of power is being consumed within the mill. Note that the energy dissipation rates quoted here are for just the particles in a single periodic slice. For a full mill, these need to be scaled by the ratio of the mill to slice lengths.

To start, we concentrate on the coarse feed case (left column of Figure 5). All the energy spectra have a log-normal-like distribution. There is a maximum energy that any particular type of collision can dissipate, typically governed by the maximum fall height of the heaviest particle involved in that type of collision. These events are very rare with frequencies typically around 0.1 per unit length of the mill. This is the equivalent of one per 10 s or once per two to three mill revolutions. Although rare, these events are fairly strong so the total energy dissipated by these is around 0.1–1.0 W. For lower energy levels the frequency of collision rises rapidly to a peak level of around 10^5 collisions/s/m at 7 mJ total collision energy. The highest rate of energy dissipation of 200 W occurs at a higher energy level of 0.17 J. From these median peaks, the collision rates decline slowly at first and then more rapidly. The combination of declining collision energies and frequencies means that the energy dissipation drops off rapidly from the peak. Figure 5 shows the spectra for the four most important types of collision in the mill. The strongest energy dissipation

DOI: 10.1002/fld

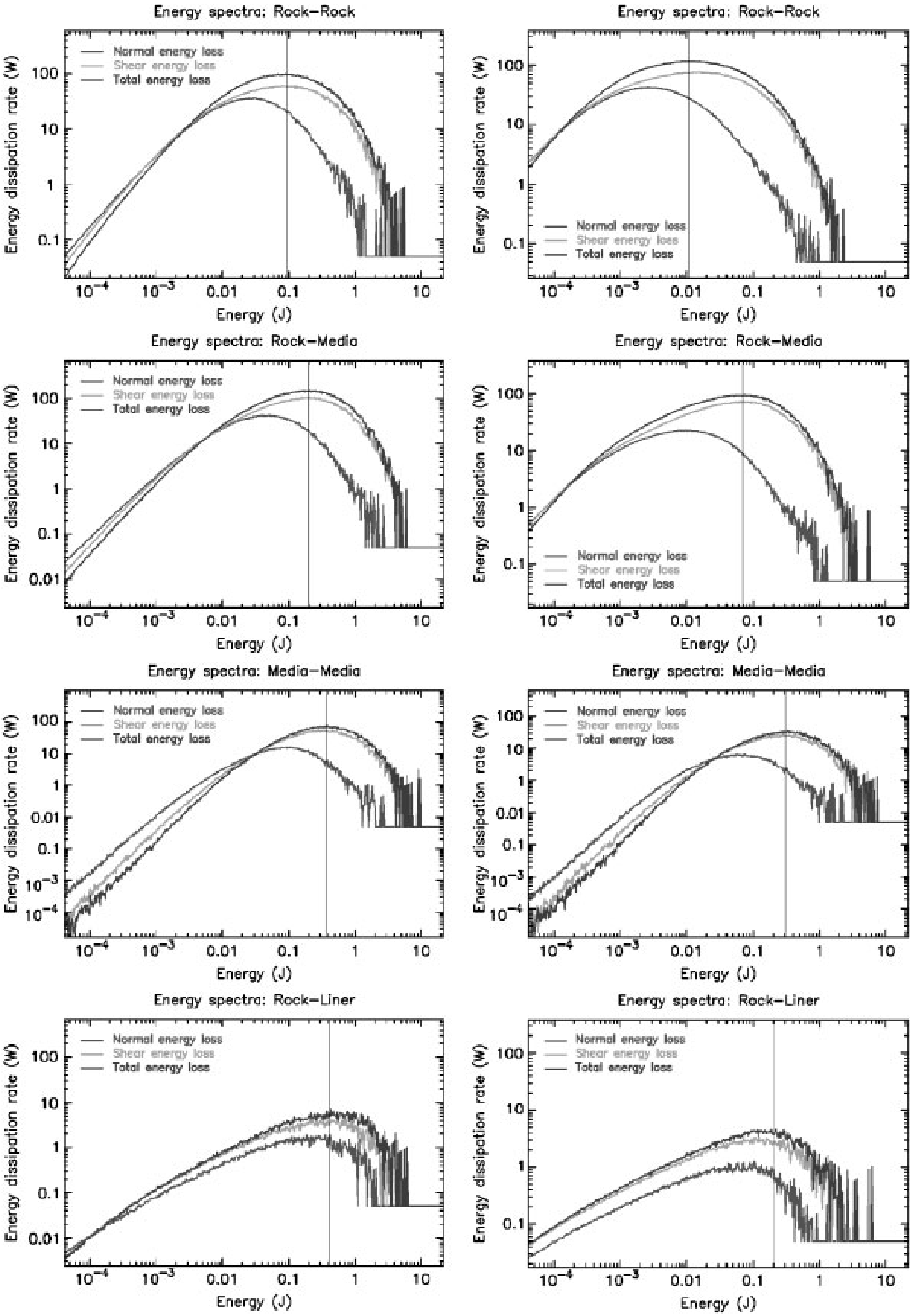

Figure 5. Energy spectra for (left) coarse size distribution and (right) fine size distribution in the cement ball mill.

rate is experienced for the rock–media collision at around 150 W occurring at an energy level of 0.2 J. The next most important energy dissipation is in the rock–rock collisions whose peak energy dissipation is 100 W occurring at 0.1 J. The next most important contribution occurs for media–media collisions with peak energy dissipation of 70 W at a collision energy level of 0.36 J. This energy contributes only to ball wear and results from a much smaller frequency of much more intense impacts (due to the large weight of the balls). Rock–liner collisions are more intense with their peak at 0.4 J but these are much less common so their contribution to the overall dissipation is only 6 W.

As was observed earlier for the SAG mill, the energy absorption is again dominated by the shear component. For all the collision types, the distribution of shear energy dissipation is very similar to the overall energy dissipation distribution with the peak shear dissipation rate occurring at between 1.0 and 2.0 times the overall level. Conversely, the normal energy dissipation is much smaller with its peak rate of dissipation being around 40% of that of the shear and occurring at collision energy levels around 10 times smaller. This again demonstrates that the energy dissipation is predominantly produced by particles sliding over each other rather than during head-on impacts. Sliding motion of the balls is the dominant mechanism leading to size reduction in the ball mill.

Comparing the energy spectra for the fine and coarse feeds (Figure 5), we observe a range of changes. The maximum energy found for rock–rock collisions declines by a factor of 2, which is smaller than one might expect since the mass of the largest rocks has decreased by a factor of 4 and that of the lightest rock by a factor of 10. This indicates that the presence of the media is having a significant effect on the rock–rock collisions by increasing the pressures involved. The highest energy dissipation rate is observed to move to a lower energy (from 0.1 to 0.01 J), which is about a quarter of what might be expected on the basis of the reduction in the product of the rock masses. The actual peak energy dissipation has increased slightly indicating that the distribution of energy dissipating collisions has become tighter.

The maximum energies for rock–media collisions have dropped by a factor of 2 (similar to the change for rock–rock) but the highest energy dissipation collision level has only declined by a factor of 3, which is again around half the level that one might expect based on the rock mass change. The peak energy dissipation rate is unchanged in magnitude but the location has moved to lower-energy levels.

The media–media spectra are broadly unchanged, with a modest reduction in the energy dissipation in the low energy tail and a slight narrowing of the spectra. This demonstrates that the ball component dominates the charge behaviour and has large impacts on the rock behaviour but the rock changes have very limited effects on the media.

For the rock–liner collisions, the maximum shear energies have declined by about one-third, whereas the normal energy has declined by a factor of 3. This indicates that direct liner impacts by larger rocks in the toe region have been substantially reduced in line with the reduction in the rock masses. The shear energy dissipation which is controlled by the pressure of the charge above the rock particles sliding along the liner only varies slightly since the ball mass is largely unchanged.

Table III shows the distribution of energy consumption by the different types of collisions in the ball mill for the two feed sizes. These values are the integrated areas under the energy spectra curves. For the coarse feed about one-third of the energy is dissipated in rock–rock collisions, with a large 46% dissipated in rock–media collisions. The media–media dissipation is also significant at 17.8%. The rock–liner and media–liner energy dissipations (leading to liner wear) are very small. For the finer feed, the fraction of energy dissipated in rock–rock collisions has jumped sharply to 51% with matching falls in the rock–media and media–media dissipation of 8 and 9%, respectively.

DOI: 10.1002/fld

Table III. Energy usage within a cement ball mill.

Collision type	Coarse feed (%)	Fine feed (%)
Rock–rock	33.5	51.4
Rock–liner	1.9	1.6
Rock–media	46.2	38.2
Media–media	17.8	8.5
Media–liner	0.5	0.2

Table IV. Distribution of energy absorption among different particle classes and the mass and area efficiencies of energy absorption for the ball mill with the coarse feed.

Class	Size range (mm)	% Total energy	% Mass	% Energy/% mass	% Area	% Energy/% area
1	+50 to −95 balls	41.21	74.30	0.555	37.27	1.106
2	+60 to −80 feed	8.44	5.15	1.639	7.84	1.077
3	+40 to −60 feed	22.82	10.27	2.221	21.66	1.054
4	+25 to −40 feed	26.33	10.28	2.562	33.24	0.792

Table V. Distribution of energy absorption among different particle classes and the mass and area efficiencies of energy absorption for the ball mill with the fine feed.

Class	Size range (mm)	% Total energy	% Mass	% Energy/% mass	% Area	% Energy/% area
1	+50 to −95 balls	27.74	74.29	0.373	24.24	1.144
2	+40 to −50 feed	7.86	3.86	2.038	5.99	1.313
3	+30 to −40 feed	15.86	6.43	2.468	12.90	1.230
4	+20 to −30 feed	22.98	7.71	2.980	21.59	1.064
5	+10 to −20 feed	24.65	7.71	3.196	35.28	0.699

This would suggest that the media used here is much better at supplying energy to the fine feed material than to the coarse and also suggests that the coarse feed will produce higher ball wear rates. The liner energy dissipation components have also dropped by 25%, which would suggest that the coarser feed will produce higher wear rates on the liner and a shorter lifespan for the liner. This comparison demonstrates that although the overall power draw for the two feeds are almost the same, the nature of the collisional environment in the charge and how this energy is dissipated is substantially different with the finer feed being better able to absorb energy with perhaps 56% absorption leading to better grinding than for the coarse feed with energy absorption of only 42%. On this fairly crude energy calculation one might anticipate a one-third increase in grinding for the fine feed (which should result in some combination of higher throughput and a finer grind).

To help understand the energy absorption by the rock, we look now at the energy dissipation in each of the size classes of the charge. Tables IV and V show the distribution of energy absorption for the different particle classes and the mass and area efficiencies of energy absorption for the coarse and fine feeds, respectively. The actual fraction of the energy dissipated is heavily dependent on the amount of that material in the mill. We therefore look at two measures of the energy absorption efficiency of each of the charge components, one based on energy absorption per unit mass and the other per unit area. From Table IV we see that the balls absorb a much lower fraction of energy per unit mass than average (around half). The coarsest fraction of rock absorbs around 1.6 times the average. This continues to increase to 2.56 for the smallest of the rock classes. Hence, the energy is dissipated disproportionately to the mass with the finer sizes absorbing more. There are a number of contributors to this including the difference in density of the rock to the steel, the different coefficients of restitution for collisions of different combinations of material and the different numbers of contacts that each particle class has with neighbours. Looking at the energy absorption per unit of surface area we find a much better correlation. The ball and first two rock classes have area efficiencies of a little over 1, meaning that they absorb energy broadly in proportion to the surface area of each class. This behaviour was confirmed in more detail in small-scale autogenous mill testing reported by Djordjevic *et al.* [30]. Relating the particle wear rate to the DEM estimate of frictional energy works quite well in these energy ranges.

The smallest rock fraction though has a much lower efficiency of around 0.8. This probably relates to the absence of smaller rock classes that make it harder to load the surface of this smallest class.

Table V shows the energy absorption for the fine feed. The trends are similar to that observed for the coarse feed. The mass efficiency for the balls has dropped to only 0.37 while the largest rock class has a mass efficiency of 2.0, which is similar to that of the matching size class in the coarse feed. The mass efficiency continues to rise with decreasing size to a peak of over 3 for the 10–20 mm class. The correlation with area is again much better with the ball efficiency being around the same level of 1.1 as was found for the coarse feed. The largest rock class has an area efficiency of 1.3, meaning it is 30% better at absorbing energy per unit of surface area than average. The area efficiency declines very slowly with decreasing size (as it did for the coarse feed). The smallest size class has an efficiency of only 0.7, which is fairly similar to the behaviour of the smallest class in the coarse feed. This further suggests that this might relate to the absence of smaller size classes.

4. GRINDING TABLE

Another grinding device, commonly used for cement grinding, is a grinding table or sometimes called a roller mill. In this particular example, a 4 m diameter table rotates around its centre at 20 rpm. It has a lip around the outside to prevent particles being thrown off. Four 1.2 m diameter rollers are positioned just above the table. They counter-rotate so that the peripheral roller speed matches the table speed at the lowest point. Particles (with diameters 25–75 mm and density $3000\,\mathrm{kg/m^3}$) are fed onto the centre of the table at a rate of 450 tph. Upon contacting the table, they are thrown outward. The lip on the edge of the table traps the particles, leading to the formation of a bed of particles on the table. Many of the outward flowing particles enter the region in front of the rolls, are drawn in by the motion induced by the roller rotation and are trapped between the table and the rollers where they are crushed due to compression. In this case, we impose a lower limit on the fragment particle size of 5 mm to ensure that the particle numbers remain computationally reasonable. The largest particles are typically the weakest and have a breakage force limit of 15 kN rising to 60 kN for the finer particles that have less remaining flaws.

DOI: 10.1002/fld

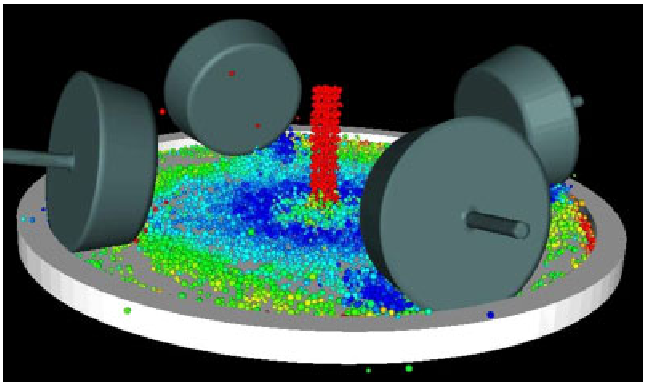

Figure 6. Grinding table rotating at 20 rpm with four equi-spaced 1200 mm rollers and a central feed shown obliquely from above with particles coloured/shaded by speed.

Figure 6 shows the flow (where the particles are coloured by speed) in such a mill once the bed depth has stabilized and the system is in approximate steady state. The incoming speed of the central feed stream is relatively fast. The particles slow as they strike the accumulated particle bed on the surface of the grinding table. As they are pushed outward, they accelerate until they encounter the rolls, are trapped and are dragged under the rolls. Here they are crushed by compression. Some high-speed fragments fly out from the rollers. Each roll generates a bow wave effect with a mass of particles building up higher in front of the roll than is found throughout the rest of the bed. Some of these particles are pushed sideways and flow around the roll forming the sides of the bow wave and some are pushed in front of the roll. The pile of material pushed along in front of the roll needs to generate enough back pressure in order to force particles under the roll. For this four-roll case, the bow wave from each roll is directed under the middle of the following roll. This would appear advantageous for particle breakage.

The DEM model used here includes a simple but effective dynamic breakage model [10] where particles reaching a critical breakage force (as determined by the DEM contact force model) are replaced by a suitable assembly of daughter particles that are then free to move independently. In this case of spherical particles fracturing into spherical progeny, a geometric packing algorithm is employed. A primary fragment is chosen and placed in the parent. The next biggest particle that can fit is added along the same axis as the first. Then layers of maximally sized finer particles are added into the biggest gaps in the previous layer. This is performed repeatedly with up to five levels of progressively finer fragments added. For more details on the progeny construction method, see [10].

For the grinding table, this means that the daughter fragment particles can then be re-trapped further under the roll and be broken again as many times as is needed for them to pass through the gap between the table and the rolls. Figure 7(a) shows the bed of particles on the table from below with the particles coloured by size (red for the largest and dark blue for the smallest fragments). The central feed and the outward flow of this coarser material (light blue to red particles) are visible in the middle sections of the table. The bow wave of coarser bed material piled up in front of and flowing around each of the rolls is also clearly visible. The compression region under the roll can also be observed with the larger particles able to approach only within several diameters

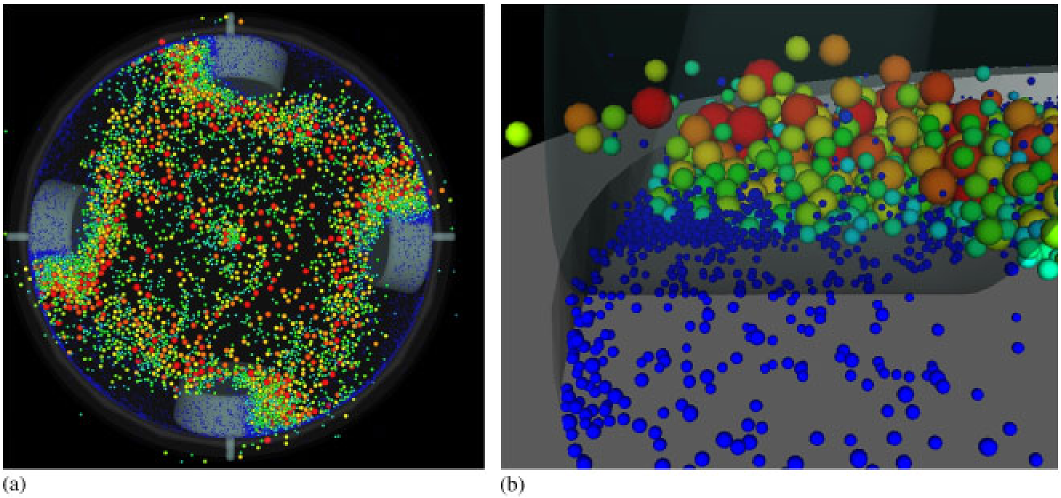

Figure 7. Grinding table with particles coloured/shaded by size shown from: (a) underneath and (b) looking through the roll at the bow wave/zone of compression breakage under the roller.

of the middle of the roll before the roll–table distance becomes smaller than the particles size and it is fractured. There is a clear gradation of size as the particles move further under the rolls. Finally, only a layer of dark blue 'product' particles is observed as the particles reach the minimum size enabled for this model. These fine fragments then pass under the roll and either join the concentrated band of fines trapped by the lip around the edge of the table or flow over this packed bed of fines and are discharged from the table as product. The discharge material commonly includes both unbroken feed and product and then needs to be separated by some type of air classification system with the coarse fraction returned to the feed stream in a closed circuit. At this stage, we do not seek to model either the ultra-fines or the coupled air flow.

Figure 7(b) shows the breakage region and bow wave in front of a roller from a view looking through the transparent roll with the particles again coloured by size. The restriction of the flow under the roller causes a bow wave of densely packed particles to form in advance of the roller. Many of the particles in the bed are pushed sideways around the roll, some being forced over the lip of the table to be discharged and some radially inwards onto the table. Some particles are dragged under the roll and rapidly crushed since the gap between the roll and the table decreases as the particle is dragged further under the roll. The fines (coloured dark blue) are free to flow out from the back of the roll.

Figure 8 shows the energy spectra predicted for the grinding table. The normal energy dissipation (typically associated with impact breakage) is shown in black and the shear energy absorption is shown in grey. It is clear that the shear energy is weighted to higher levels than the normal energy. Measured over all collisions, the normal impact energy accounts for 35% of total energy consumption while the shear dissipation accounts for 65%. The shape of the energy spectra is noticeably different to those of the ball mill (see Figure 5) even when considering the different minimum energy thresholds used in the plotting. This indicates that there are important performance differences between the two types of mill even though they are often used for the same cement

DOI: 10.1002/fld

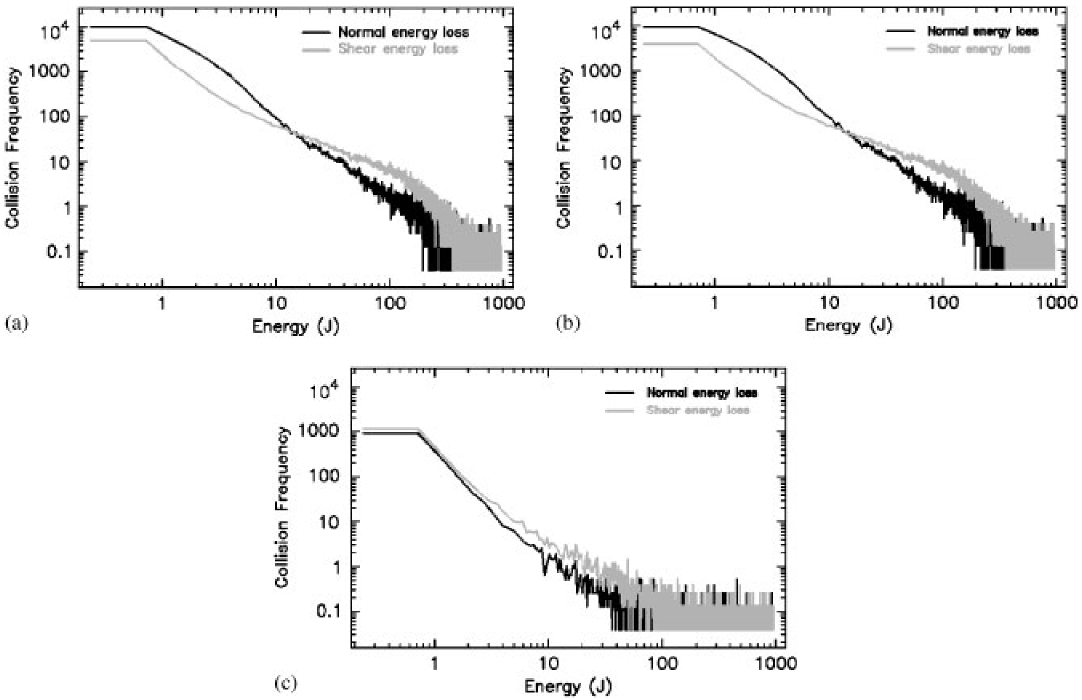

Figure 8. Energy spectra for the grinding table: (a) over all collisions; (b) from rock-grinding table and rolls; and (c) from rock–rock collisions.

applications. The energy spectra for the collisions between the particles and the grinding surfaces (tables and rolls) are very similar to the spectra for all collisions. The spectra for the particle–particle collisions though are quite different. The collision rates are much lower as are the average levels of energy dissipation (around 10 times lower) but there is also a long tail of high-energy events. These occur between particles in the compression zone as they are loaded under the rolls. The rate of these collisions is low but they are an important part of the breakage and energy consumption process.

Note that the smallest particle size can become jammed under the rolls in an unphysical manner because of its inability to break and so can absorb unrealistic amounts of energy. Hence, ideally the minimum particle size used in the model should be less than the separation of the rolls from the table (i.e. less than the bed depth under the rolls). This will allow more accurate prediction of the energy absorption by the smallest class and therefore more accurate predictions of the power draw.

Figure 9 shows the distribution of energy absorption across all the breakable size classes. The largest particle sizes absorb only around 5% of the energy (despite being around 10% of the particle mass). The rate of absorption rises almost linearly for particle classes down to 40 mm diameter. At this size, the particles absorb around 10% of the energy and represent 10% of the particle mass. For smaller sizes, the energy absorption rises sharply, with 27% of the energy absorbed for the smallest of these size classes. The particle sizes used in this grinding mill simulation are

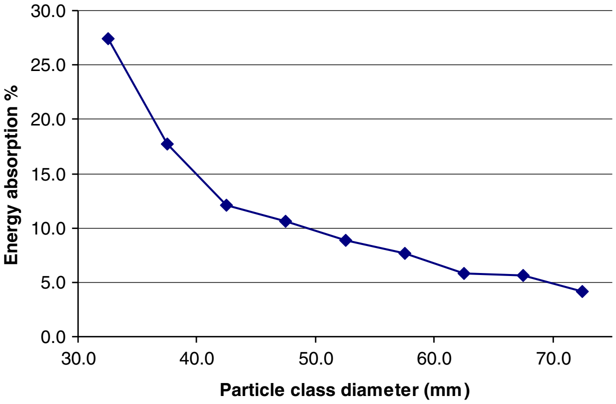

Figure 9. Distribution of energy absorption across all the breakable size classes.

very similar to the ones used in the coarse cement ball mill discussed earlier. The distribution of energy absorption with particle size is remarkably similar for the two machines (see Table IV for the ball mill results) with the % energy/% mass being around 0.5 for the largest particle sizes and increasing to around 2.5 for the finest. This suggests that the rate of energy absorption for the grinding table is again controlled by the total surface area of each size class.

Figure 10 shows the rate of fracture of the particles and the rate of product creation by the mill. The overall rate of fracture is quite variable with high-frequency fluctuations, depending sensitively on the specific particles being trapped under the rolls. The overall rate varies between 250 and 450 fracture events per second. The fracture rates are smallest for the largest particles (since there are relatively few of these per unit mass). Figure 10(c) shows the fracture rate for the largest size with an average rate of 2 fractures/s. The breakage rate increases with decreasing size. For class 7 (55–62 mm) the rate has increased to 5 fractures/s. For class 4 (30–36 mm) the much larger numbers of particles available mean that breakage is more continuous, albeit still with wide fluctuations and with an average of around 50 fractures/s. For the second smallest class, the fracture rate has risen to 130 fractures/s. The fracture rates are clearly dependent on the number of particles in each size class and also on their breakage strength. DEM is able to predict not only the energy consumption, the pattern of usage of that energy, but also the breakage outcomes. This work demonstrates that DEM models can, in principle, make predictions of the resident size distributions and product size distributions of mills. Determining how realistic these predictions are and refining the dynamic breakage models to improve them are the subject of ongoing work.

For the current grinding table configuration, with its relatively light bed loading and for the material hardnesses chosen, the product generation rate predicted is about 11 kg/s or about 40 tonnes/h. The power draw measured was 65 kW with 25 kW being supplied by the grinding table and 10 kW supplied by each of the four rolls. This size of table can be run with much higher bed loads so as to generate product at rates up to 400 tonnes/h. Scaling up the power similarly would lead us to expect a power draw of around 650 kW. This is around 6 times lower than the typically installed power. This leads us to expect that truncating the product size distribution may lead to under-prediction of power draw for these types of compressive mills since much of the finer breakage occurring in

DOI: 10.1002/fld

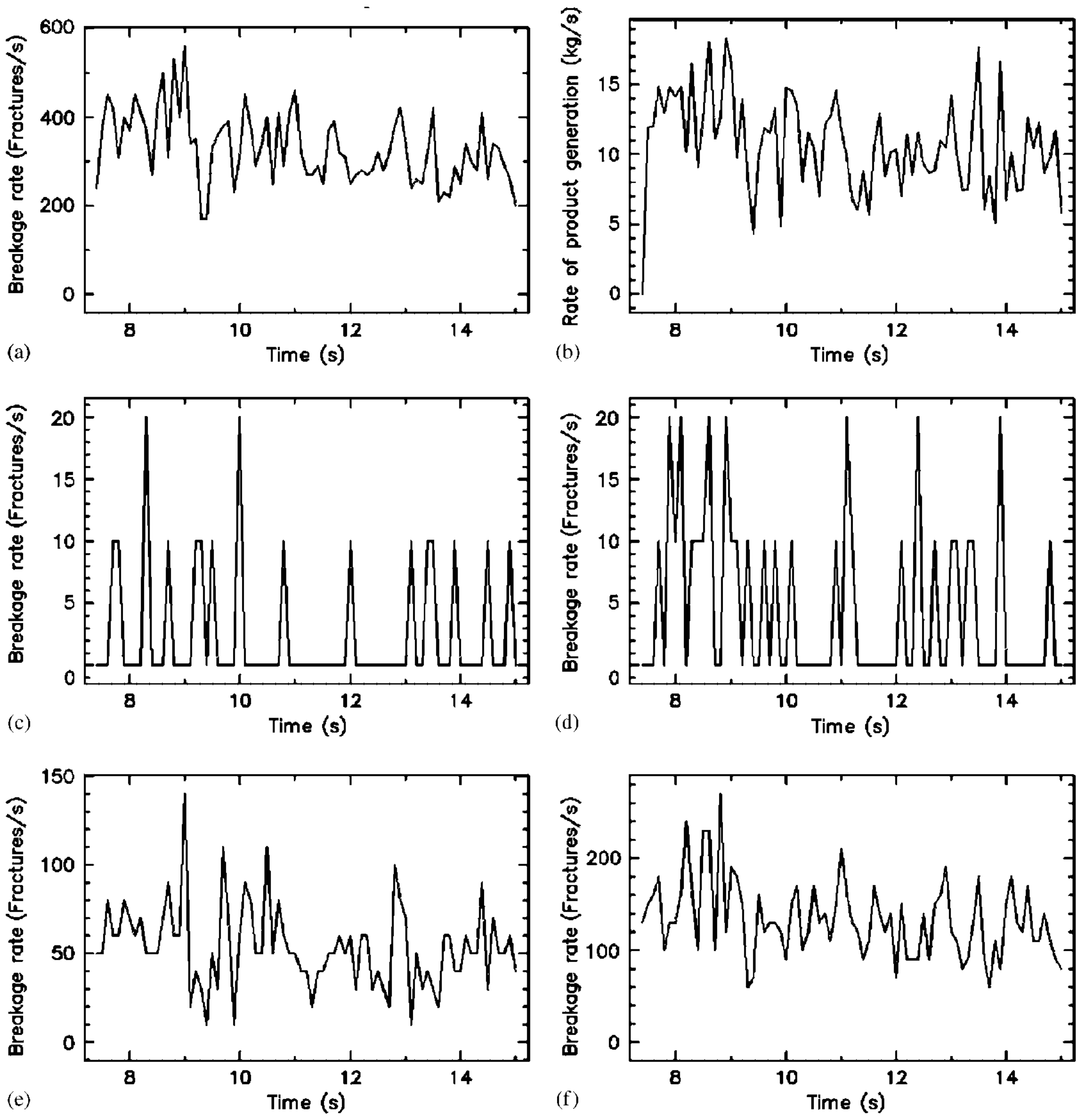

Figure 10. Particle breakage predicted for the grinding table: (a) overall rate of fracture events for all particles; (b) the rate of product generation (given by particles in the smallest class); (c) biggest class of particles (class 10); (d) class 7; (e) class 4; and (f) class 2 which are the smallest particles allowed to fracture by the model.

the real mill is not well represented in the model with this choice of minimum particle size. This suggests that quantitatively accurate prediction of all mill outputs may require resolving more of the finer end of the size distribution. This is becoming increasingly feasible as computer power increases. More investigation is needed to clarify these issues.

5. STIRRED MEDIA MILLS

Stirred mills are becoming increasingly used for fine and ultra-fine grinding. This technology is still poorly understood when used in the mineral processing context. This makes process optimization of such devices problematic. Three-dimensional DEM can again play a part in understanding the fundamentals of particle size reduction and media behaviour inside these mills. In this section, we present examples of DEM simulation for two fine-grinding mills.

5.1. Tower mill

A tower mill has a vertical cylindrical shell and employs a vertical double helical steel screw agitator located along the axis of the mill shell. The mill is substantially filled with grinding media (typically steel or ceramic balls). The screw agitator stirs the media while simultaneously lifting and circulating it throughout the mill. Fine feed material is introduced at the top surface of the charge and is circulated throughout the mill where it is ground by being crushed or sheared between media particles. The rotation of the screw creates centrifugal forces that compress the charge radially outwards. This is balanced by gravity. The screw rotational speed is limited by the need for the vertical force resulting from the centrifugal compression to remain smaller than gravity so that the charge is not lifted out of the mill, (see [31] for more details). The rotational speeds and therefore the energy intensity produced within the tower mill is much higher than for a ball mill (with a speed differential here of around a factor 6) and so a tower mill can typically produce a much finer product. The nature of the flow pattern of the media and manner of energy dissipation within the mill though is not well understood.

Here we model a tower mill filled with dry ceramic media. A coefficient of restitution for the media of 0.3 is used (to take account of the fine powder being ground that will occupy the interstices between the balls in the mill). The friction coefficient was chosen to be 0.5 for media–media and media–liner collisions. The fine feed material which is intended to be ground by the mill is too small to be able to be included directly in the DEM model and is omitted. The grinding media, which are typically 1–2 orders of magnitude larger, can be fully included. A spring constant of $10\,000\,\mathrm{N/m}$ was used giving average overlaps of about 1%. Key geometric details and operating parameters for the tower mill are given in Table VI. The details of the ball charge are given in Table VII. The mill is filled nearly to the top and contains around 30 000 media particles.

Figure 11 shows the distribution of the media in the tower mill once it has reached the steady state. The mill and charge have been cut away to allow us to see inside. Figure 11(a) shows the media coloured by speed. There is a solid core of media, occupying a large fraction of the mill vessel, which moves with the screw agitator and which is coloured green. Near the outer edge of the screw (which is the most rapidly moving part of the screw and the part that encounters the highest collision intensity) the media particles are driven faster, with particles achieving double the average core speed (and coloured yellow to red). Around the central moving core is a fairly clearly defined layer of slow-moving particles that are adjacent to the cylindrical mill shell. Frictional drag slows these particles. The sharp change in speed from the slow outer layer to the inner core means that there is significant shear in the narrow transition region between the blue and the green particles, which will lead to significant abrasive wear.

Figure 11(b) shows the same particle distribution but now coloured by the amount of energy that each particle has absorbed from the normal component (head-on impact) of the collisions that they have experienced. There is a clear gradient in the energy absorption with the highest levels (which

DOI: 10.1002/fld

Table VI. Key details of the tower mill charge.

Number of particles	29 870
Particle density	2700 kg/m^3
Total particle mass	58.4 kg
Spherical particle size	−14 to +9 mm

Table VII. Specifications of the tower mill used in the DEM simulations.

Rated power	1.5 kW
Angular speed	100 rpm
Chamber volume	39 l
Stirrer	Double helical steel screw
Chamber diameter	0.24 m
Chamber height	1.2 m
Stirrer diameter	0.14 m
Pitch	0.09 m

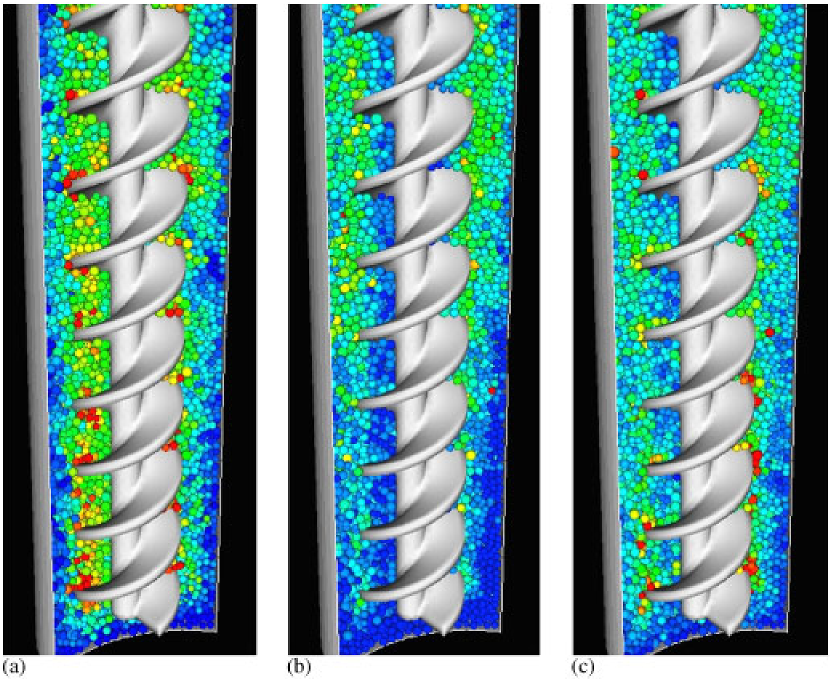

Figure 11. Three-dimensional flow pictures showing a clipped section of the tower mill. Media particles are coloured by: (a) speed with red representing a speed of 0.5 m/s; (b) normal energy absorption rate with peak values (red) of 7 mW; and (c) shear energy absorption rate with peak values (red) of 20 mW.

will correspond to regions of high-impact damage for the fine feed material that occupies the space between the balls in the real mill), with the highest levels found at the top of the mill and the lowest levels at the bottom. This occurs because the screw agitator is actually a very effective transport device and lifts the media in the core of the mill upwards, producing higher pressures at the top of the mill and therefore more intensive impacts. Figure 11(b) shows the distribution of the shear energy absorption in the mill, which will correspond to the intensity of abrasive size reduction of the feed material. There is still a vertical gradient present with the highest values found at the top of the mill, but it is much weaker than for the impact (normal) energy absorption. The reason for this is that the Coulomb limit on the frictional force is proportional to the normal load. The shear energy absorption is a product of the shear force and the shear velocity. The vertical gradient in the normal force therefore creates a matching gradient in the shear component. However the shear velocity also contributes. Looking at the speed distribution (Figure 11(c)) we see that the transition from slow-moving blue material around the shell to fast-moving core material is much sharper at the bottom of the mill than at the top. Therefore, the shear rate is higher at the bottom than at the top. This increases the shear energy dissipation at the bottom of the mill. The mild vertical gradient in the shear energy absorption is therefore a balance between the normal force, which increases with distance from the bottom and the shear rate which decreases.

One way of characterizing the flow in this type of mill is to calculate averaged one-dimensional profiles of the velocity components, as a function of mill height and radius. These are shown in Figure 12. The velocities are collected in radial and vertical slices of the mill to calculate a mean velocity and standard deviation for each radius and height. The mean radial velocity is statistically zero over most of the mill height. Near the base of the mill, it has a small but meaningful negative value, indicating that the particles are flowing from near the outer mill chamber radially inwards towards the central screw. Near the free surface, the radial velocity becomes significantly positive as particles flow back from around the screw, outwards towards the outer mill shell. The standard deviation is a measure of the variability of the velocity from its means and of the extent of fluctuations in the flow. The standard deviation is much larger than the peak values of the radial velocity and is constant with height. The bounding envelope, defined by the limits of the vertical lines, indicates a region of phase space which is symmetric around zero that the particle radial velocities are likely to occupy. There is no meaningful mean radial velocity at any radius. This means that in any vertical column of particles there is equal radial movement in both positive and negative directions. The outside of the screw makes the largest contribution to driving the flow and also drives the fluctuations in the flow.

The mean tangential or swirling velocity is low at the base of the mill and increases steadily over the bottom quarter of the mill. The swirling motion is then essentially constant over most of the height of the screw. There is a strong drop in the particle swirl in the top surface layers of the charge where the particles are more mobile and move out towards the mill shell. The variability of the swirl speed is also quite constant over most of the mill height, except in the surface layers. The tangential speed variation with radius is very strong. It is zero for radii less than or equal to 0.02 m since this is the radius of the core of the screw and particles cannot be found at these positions. The swirl is low near the core of the screw ($r>0.03$) and increases strongly and monotonically with mill radius up to a peak at the edge of the screw ($r=0.07$). It then decreases almost linearly with radial distance out towards the mill chamber wall. There is a reasonable degree of slip experienced between the charge and the wall at about a third of the peak tangential speed.

The mean axial velocity is statistically zero at each height and the amount of variability in the instantaneous axial velocities is also constant with height. Since the screw and chamber

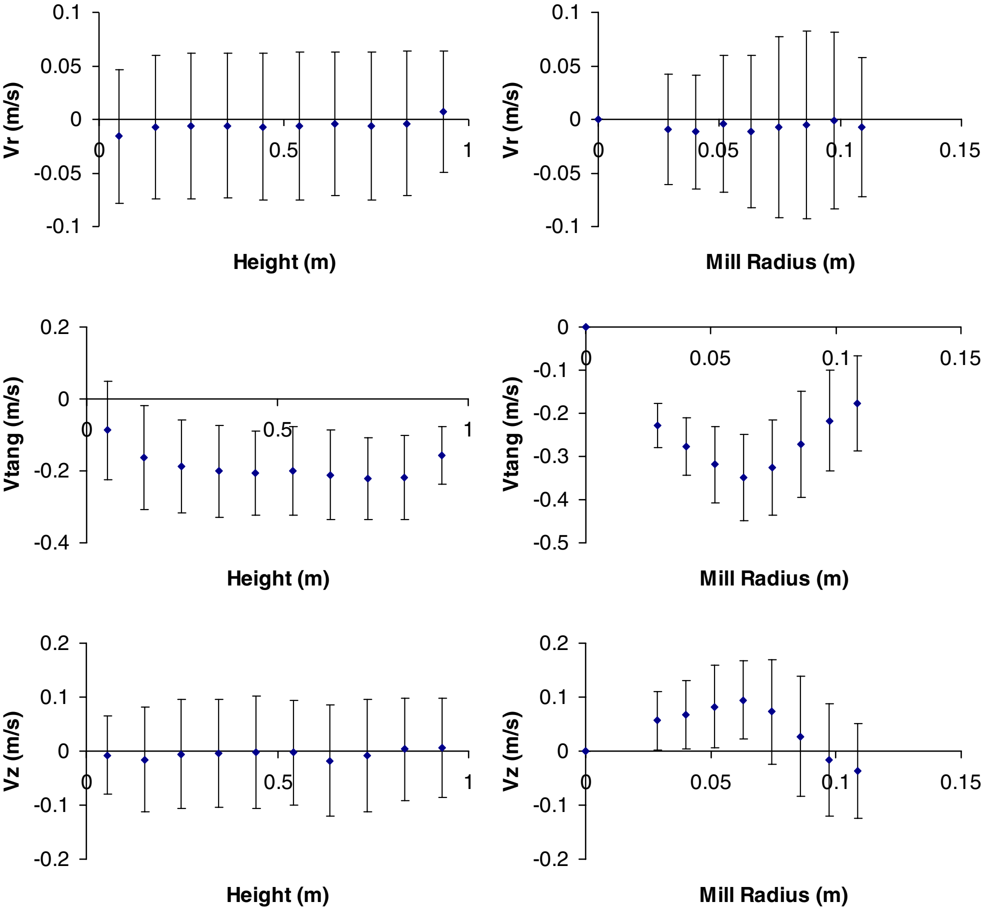

Figure 12. One-dimensional profiles of media velocity (Vr, Vtang, Vz) *versus* mill height and radius for the tower mill at $t=10$ s. Confidence limits of one standard deviation show the variance in velocity. The radius of the screw is 0.07 m and the chamber radius is 0.12 m.

cross sections do not vary with height, this means that in any axial slice there is, on average, as much material moving down the mill as there is moving up the mill with the screw motion. In contrast, the mean axial velocity varies strongly with radius. It has intermediate values within the screw, which increase moderately with radius to a peak transport rate at the outer edge of the screw. The mean axial velocity then drops almost linearly to a point just inside the mill shell. From a radius of around 0.09 m, the mean axial speed is negative, indicating that there is strong coherent down flow in an outer annular region that is about 25% of the radius of the mill chamber. The average speed of the outer down flow is much slower than that of the inner up flow because the mass flow rates must be equal (since this flow is in equilibrium) and the outer annulus has a much larger large cross-sectional area. The downward mass flux through this outer cylinder therefore matches the upward flux in the inner core.

Combining the interpretations of the radial and axial mean velocity fields, it is clear that there is a strong global recirculation pattern within the tower mill driven by the screw motion. Particles are transported upwards by the screw in a central cylindrical core. As they approach the free surface, they begin to flow outward towards the mill shell. Once they are further out than 75% of the mill radius, they begin to flow somewhat erratically downwards in an annular down flow region around the outside of the charge. At the bottom of the mill, the particles flow back in towards the screw where they are again picked up and transported upwards by the screw.

To understand the nature of the energy utilization in the tower mill, we calculate one-dimensional profiles of the energy absorption rate as functions of mill height and radius. The distribution of energy absorption by the media indicates where in the mill the particle size reduction of feed material is occurring. Figure 13 shows that mean energy absorption rates for normal, shear and total energies are largely insensitive to axial position in the mill, except right at the bottom of the mill

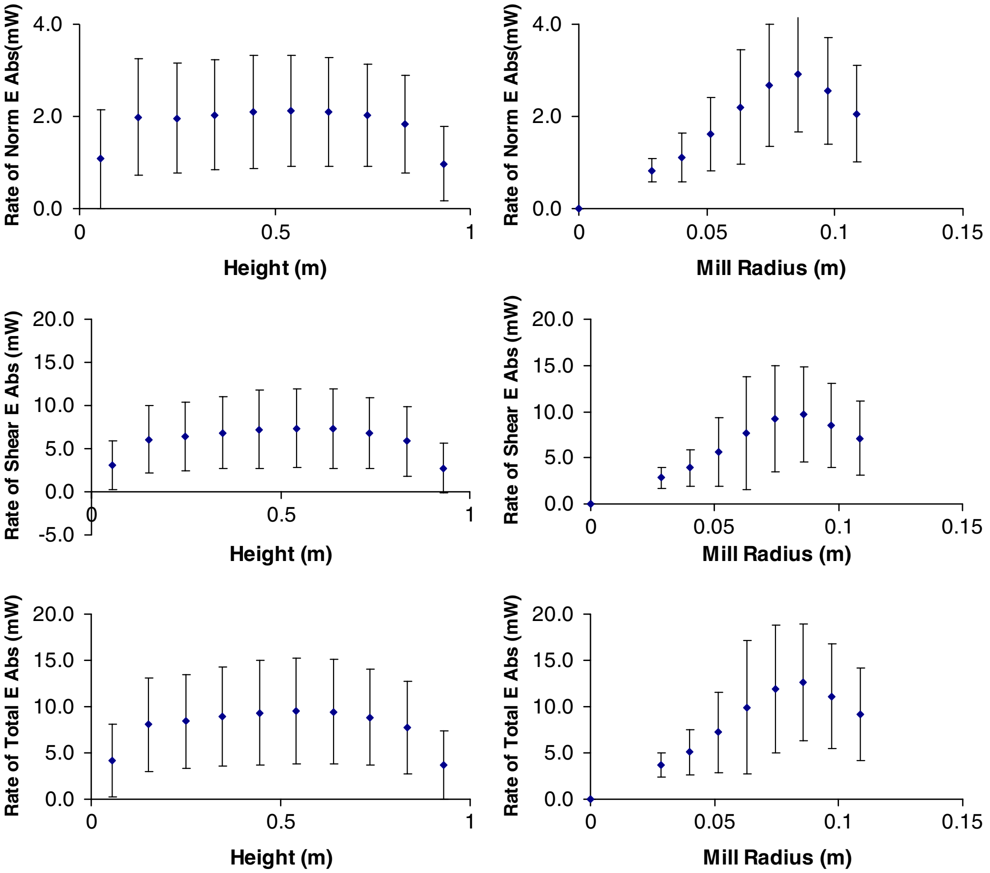

Figure 13. One-dimensional profiles of media energy absorption rates *versus* mill height and radius for the tower mill collected over only two revolutions when in steady state. Confidence limits of one standard deviation show the variance in velocity. The radius of the screw is 0.07 m and the chamber radius is 0.12 m.

where they are lower because the screw impeller does not reach down to the floor of the mill. The energy absorption by the media declines reasonably strongly over the top third of the mill. The shear energy absorption in the bulk of the mill also shows a modest increasing trend with increasing height. The mean energy absorption rates all have strong radial dependence. They are relatively low at small radii near the shaft of the screw since the centrifugal forces are smaller here. The energy absorption rates increase rapidly with radii and reach peak values at about 0.085 m, which is moderately outside the outer diameter of the screw and well beyond the location of the peak axial velocity. This is the region of highest shear between the upward- and downward-directed streams of particles. Energy absorption then decreases with increasing radius but is still significant all the way out to the mill chamber wall.

The average power draw for the tower mill was predicted to be 0.27 kW. For more details of the media motion and energy consumption in this tower mill see [31] and for details of mixing and transport [32].

5.2. Isamill

The Isamill is a horizontal stirred mill with multiple grinding discs on a central rotating shaft. Since it has a closed grinding vessel and does not rely on gravity to keep the mill charge within the mill, significantly higher rotational speeds can be used for this mill. Speed increases of factors of 10–20 are possible. The much higher speeds produce centrifugal forces that are 100–400 times higher, leading to much higher pressures, much higher shear rates and much higher levels of energy consumption for breakage. This type of mill can be used for ultra-fine grinding with product sizes down to a few microns possible. These very fine products can often be produced at favourable energy consumption rates if well tuned to the material being ground. The stirring agitator used is a shaft with several discs attached at regular intervals along the shaft. These extend most of the way to the outer cylindrical shell. Typically the discs have 4–6 holes (passing completely through the disc) with circular or elliptical shapes regularly spaced around the discs at about half the radius of the disc. The mill is filled to 75% volume with a charge composed mostly of grinding media (which could be steel or ceramic balls, sand or fine slag). The discs partition the charge into distinct zones or compartments and the disc rotation generates recirculating motion of the grinding media within and between the compartments. Fine feed material is added at one end under high pressure and is transported along the mill, being progressively ground by the media and then ideally discharged at the other end. The media is retained in the mill by a centrifugal separator.

Here, we model just one compartment around one of the discs of a laboratory scale Isamill using periodic boundary conditions in the axial direction. The mill details are given in Table VIII. The mill has a diameter of 337.5 mm and the periodic slice is 200 mm (being the centre to centre spacing of the discs along the shaft). Details of the grinding media and the feed ore are also given in Table VIII. We wish to understand the distribution of ore within the charge so feed particles need to be included in the simulation. The feed ore is represented as 1 mm particles which are over-sized compared with the actual 0.2 mm feed of interest. Since these particles are small compared with the 6 mm grinding media, this is expected to give reasonable predictions for the spatial distribution of feed. We would not expect this approach to be reasonable for predicting the breakage of the feed particles by the media.

Figure 14 shows a side view of the periodic slice of the Isamill. The mill is sectioned to allow viewing inside the charge. The 6 mm media are shown as blue and the 1 mm ore particles are shown

Table VIII. Isamill configuration, charge and operating conditions.

Mill shell radius	168.75 mm
Grinding discs	145 mm radius disk 25 mm thick 30% cross-sectional area open to flow (provided by 4 circular holes)
Shaft diameter	25 mm
Grinding media	6 mm balls with density 2700 kg/m^3
Media volume of the charge	80% v/v
Ore feed	1 mm and 5100 kg/m^3
Ore fraction of the charge	20% v/v
Charge volume fill	75%
Shaft/disc speed	1315 rpm
Disc tip speed	20 m/s

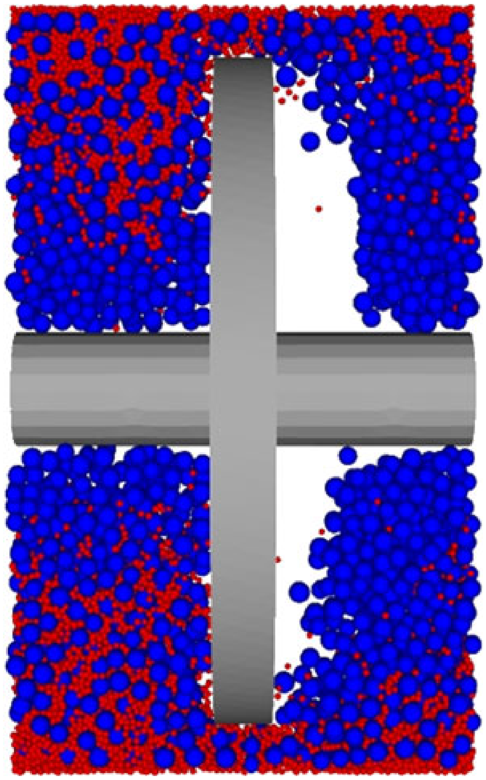

Figure 14. Media (blue) and fine feed material (red) distributions at steady state in an Isamill. The feed material segregates rapidly to the outside filling the interstitial gaps between the media particles.

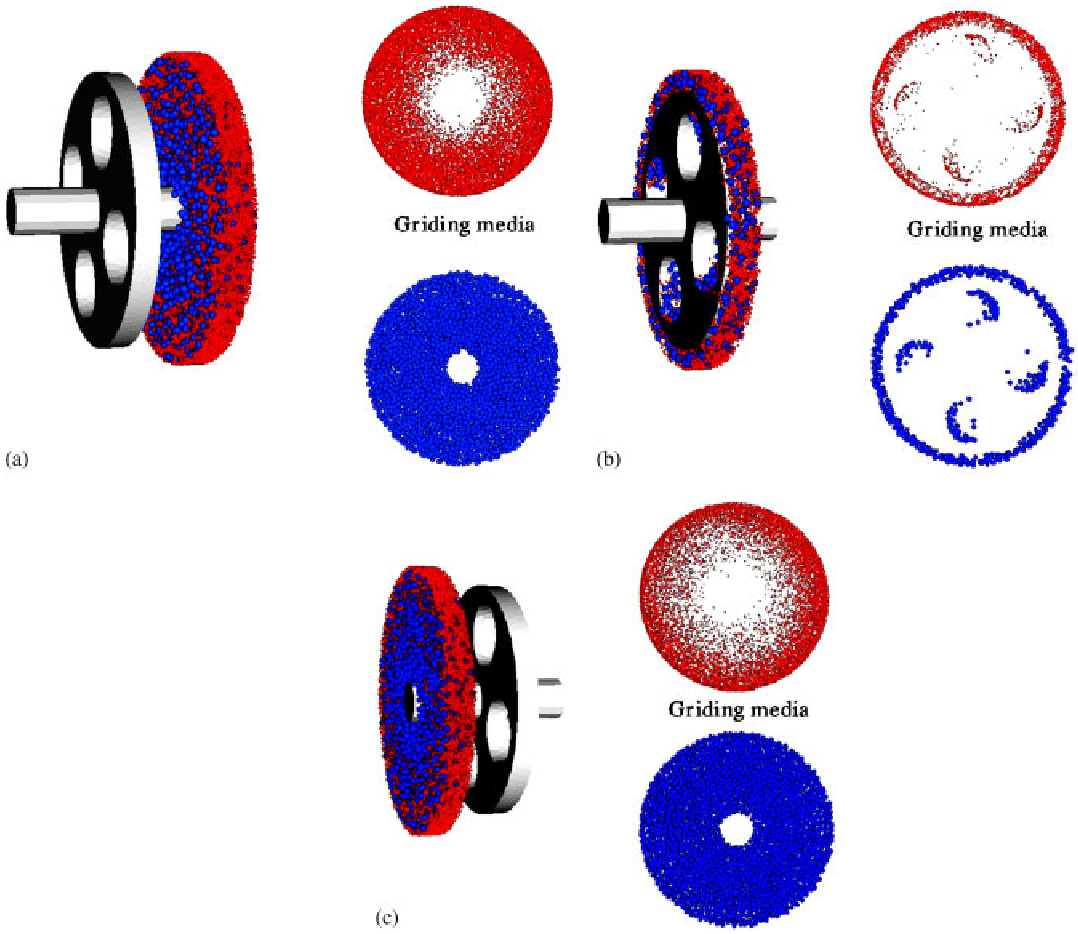

Figure 15. Grinding media (blue) and feed ore (red) distributions in different slices of the Isamill, showing: (a) slice at the feed end just before the grinding disk; (b) in a slice aligned with the grinding disk; and (c) in a slice on the discharge side of the grinding disk.

as red. The pressure gradient on the charge (implemented as an axial body force) pushes particles against the left side of the disc and leaves a matching void on the right side. The media densely packs the mill in all locations except in this void. The feed material distribution is more complex. The centrifugal force is extremely high and pushes these particles outwards. Since the feed is so small compared with the media, it is relatively free to migrate through the void spaces between the close-packed media particles until all the pores are densely filled, starting from the mill shell and moving inwards. Once in steady state, the distance that the ore particles penetrate in towards the axis of the mill is then determined by the feed ore volume fraction. A full mill can be pictured by placing several copies of this periodic slice along the axial direction. The periodic nature of the computational domain does not require the spatial distribution of charge to be uniform in the axial direction within an individual periodic region. The distribution along the mill is periodic (not uniform) with successful dense zones on the feed sides and void zones on the discharge sides of each of the grinding discs.

Figure 15 shows axial slices of the mill charge at three locations along the axis of the mill. The first one lies in the feed side of the mill compartment and shows densely packed media reaching in to the location of the shaft. The ore densely fills the voids around the outside of the mill and extends inwards for a reasonable distance. The interface is not smooth at the edge of the ore since the recirculation of the media (which is comparatively slow compared with the speed of the fines migration) causes some mixing in the interface region. The second slice is at the location of the disc. The media and ore are both confined to the narrow annulus around the outside of the disk. The locations of the four circular holes in the disc can be identified by the presence of some media and ore particles that are currently located in the openings, being moved around circumferentially by the disk. The third slice shows the charge distribution part way along the discharge side of the periodic volume. The media still densely fills the space between the shaft and the shell, but the amount of feed material is much reduced because of the restriction to axial transport that the disc represents. The ore particles are again densely packed from the shell inwards but now extend only about half the distance towards the shaft. The interface is also more diffuse than on the feed side.

It is also useful to understand the nature of the particle motion in different regions of the mill charge. To do this, Figure 16 shows individual trajectories for selected media and rock particles. The trajectory thickness is drawn to match the diameter of the particle (hence, thick curves are for media particles and thin curves are for the fine rock particles). Figure 16(a) shows a media particle between discs at a moderate radius from the shaft. This particle executes close to circular motion with some axial motion (which appears to be of the random walk type rather than a coherent axial flow). Figure 16(c) shows a similar trajectory for a particle at a large radius near the outer shell. It again follows an almost circular path. Figure 16(e) shows a media particle at a similar initial radius but starting closer to the disc. The particle follows a clear spiral pattern, moving with a reasonably steady axial speed past the grinding disc and into the next compartment between discs. Figure 16(b) shows a feed particle starting in a similar location to the media particle in Figure 16(e). It also moves in a coherent spiral pattern past the outside of the grinding disc into the next compartment. This shows that there is a coherent axial flow along the mill at radii larger than the discs. Figure 16(d) shows another trajectory for a feed particle that starts at a smaller radius. This particle moves in a spiral pattern but with increasing radius. This demonstrates that the axial flow extends some distance into the space between discs and that particles are able to migrate outward and then spiral past the grinding disk. Figure 16(f) shows a feed particle that starts at a similar radius but further from the disk. This particle travels on an essentially closed circular path with small random walk variations in the axial and radial directions. Many cycles of the rotation are shown to establish that the path is a stable closed trajectory.

Figure 17 shows multiple trajectories of some other media and rock particles within the Isamill. In the top picture, one media and one feed particle are shown together. The media particle lies on a stable closed trajectory, whereas the feed particle trajectory spirals in the axial direction with the radius of the circulation decreasing once the particle has passed the centre disc and finally passing through one of the holes in the next grinding disk to the left. This demonstrates that small changes in the particle position can lead to significant differences in the trajectories and also demonstrates the flow of particles through the grinding disc holes. Figure 17(b) shows some additional media trajectories that spiral past the outside of the grinding disk. The range of variation of the particle trajectories is substantial and occurs for only small changes in the particle starting positions. This demonstrates that the velocity field for the charge is spatially complex and presents significant

DOI: 10.1002/fld

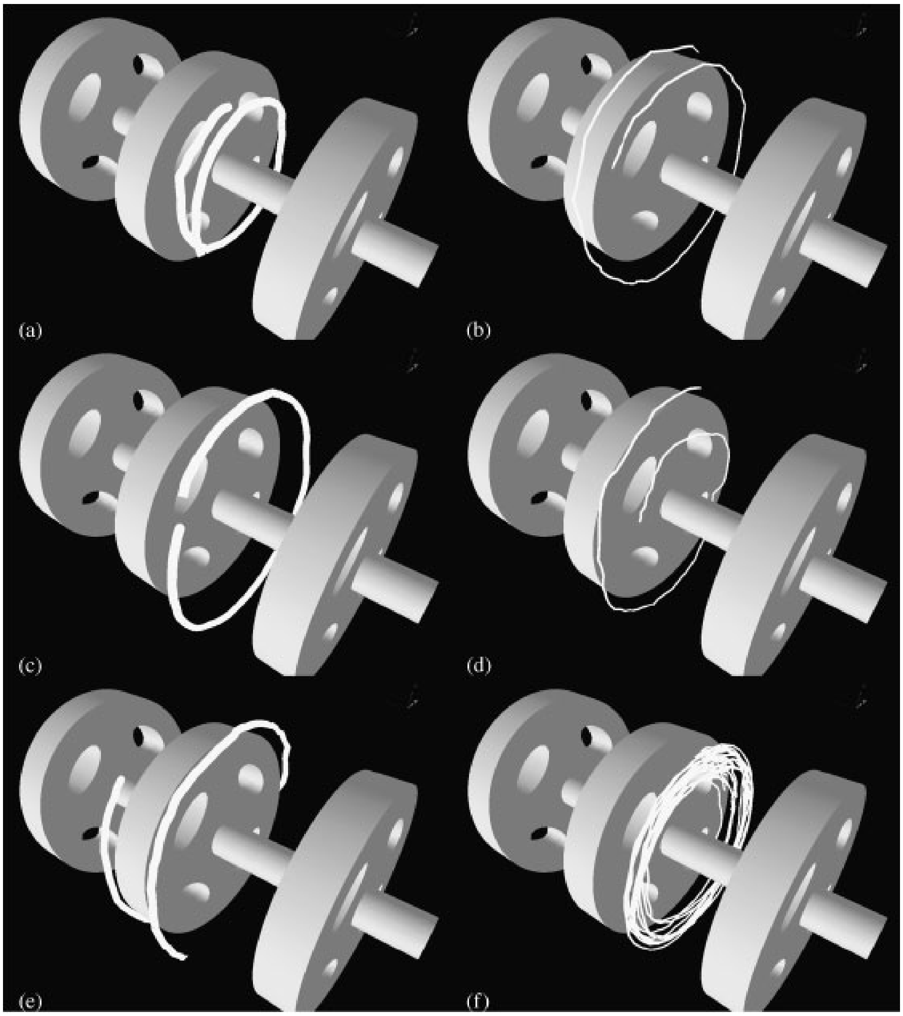

Figure 16. Selected individual trajectories of particles within the Isamill (left) media trajectories and (right) rock trajectories.

challenges for visualization and interpretation. Trajectories allow the phase space to be sampled but they are not suitable for detailed analysis of the entire velocity field. It is not clear at this point if the velocity field is steady or if there are important transient variations associated with these various types of motion. If the velocity field is steady then spatially averaging the velocities onto an Eulerian grid is one approach that can be taken to help in analysing the velocity field.

Figure 18 shows the energy spectra for this Isamill configuration. They appear to be skewed normal distributions. The collision energies range from 10^{-7} up to 2000 J. Compared with the ball mill (in Figure 5) the peak energy levels are increased by a factor 200, demonstrating the significant increase in energy intensity obtainable for such high super-critical mill rotation speeds. The minimum collision energy tail also extends down to much lower energies (10^{-7} J), indicating

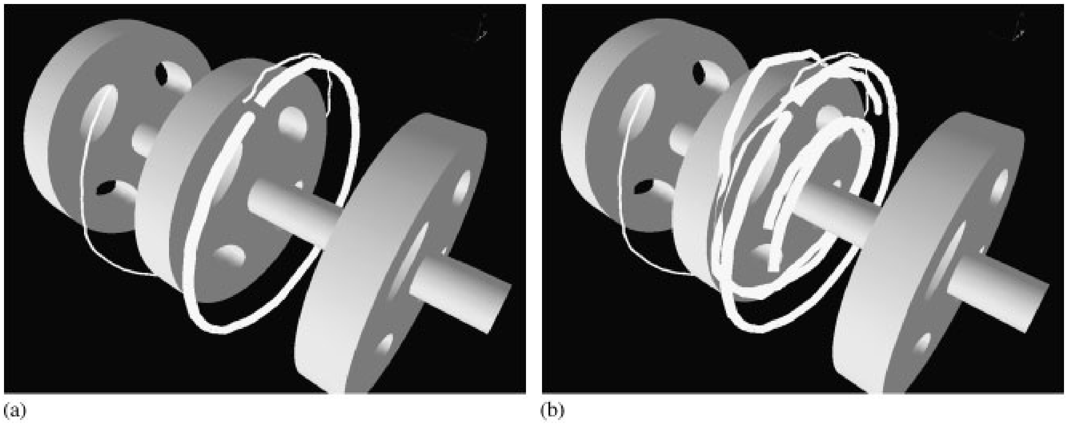

Figure 17. Multiple selected trajectories of media and rock particles within the Isamill.

that in regions of the mill the conditions are relatively benign with many very weak collisions occurring.

Considering the rock–rock energy spectra, we find that for the shear energy, dissipation has a similar shape and energy dissipation level to that of the overall spectra, but significantly reduced normal impact energy levels (by a factor of around 200). In contrast, the normal and shear energy absorption spectra are quite similar for the media–rock collisions. Looking carefully at the normal energy spectra for all collisions, we observe a clear double peak. From the sub-spectra, it is obvious that the first peak arises from the rock–rock collisions and the second higher energy peak arises from the media–rock collisions. The rock–liner spectra cover a similar range of energies but the distributions are more symmetric with the modal peak moving from around 1 J down to around 0.5 J. The frequency of the highest energy collisions also decreases from around 600 collisions/s to only 10 collisions/s, leading to more than a factor of 100 lower overall energy dissipation for rock–liner collisions. This indicates that rock collisions with the mill chamber and grinding discs are unimportant to breakage.

The media–media spectra are very similar in structure to the media–rock spectra with the normal and shear energy dissipation being reasonably similar. The modal peak energy level is around 4 times higher for the media–media collisions but the collision rates are around 50 times lower. This means that the total media–media energy dissipation is around 10 times lower than that of the rock–media. The higher energy levels of these collisions are understandable given the larger masses of the media particles. The significantly reduced collision rates for the media–media contacts reflects the effectiveness of the finer feed particles in separating the media particles. Each media particle is typically densely surrounded by a collection of small rock particles that limit direct media–media contact. This is a substantial part of the reason why such a stirred mill is able to be effective as a grinding device. The small interstitial particles are very effective at isolating the media particles and ensuring that the vast bulk of the energy is dissipated in collisions involving feed particles leading to their comminution and thereby reducing the media wear rates as well. If this was not true then the majority of the energy would be expended grinding the media rather than the feed. For this mill configuration, the energy wasted in direct media–media grinding appears to be around 10 times lower than the energy expended in collisions involving feed material. This also demonstrates

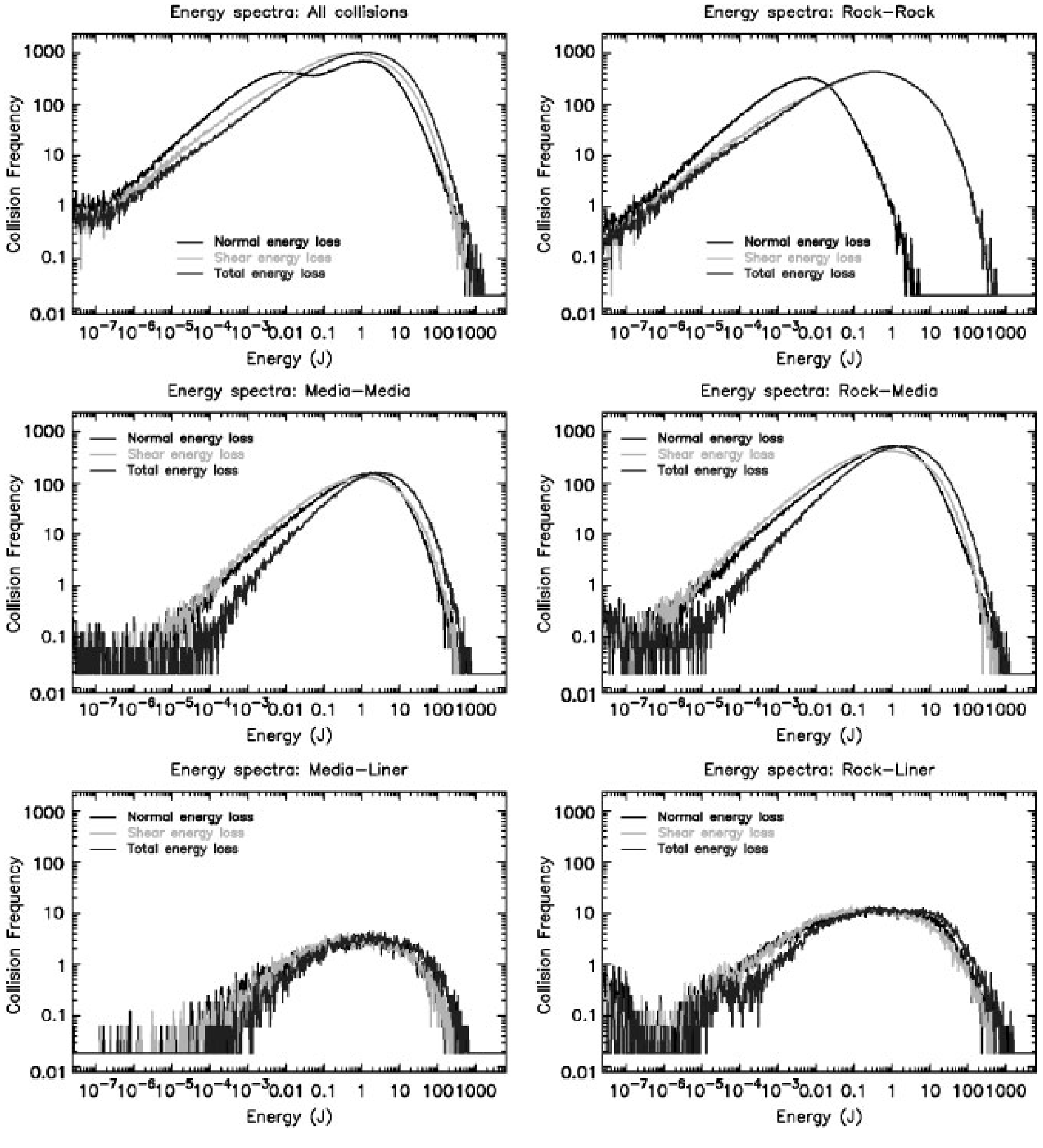

Figure 18. Energy spectra for the Isamill.

the importance of including the feed material in such simulations as they can radically alter the pattern of energy utilization in the mill model. Finally, we observe that the media–liner collisions have a symmetric profile much like the rock–liner ones but with a higher model energy peak (due to the larger particle mass) and with a much lower collision rate (due to lower numbers of these particles and their insulation from the liner by interstitial feed material).

6. CONCLUSIONS

DEM modelling has now reached a level of maturity where simulations of the order of 100 000–2.0 million particles, in realistic geometries, are feasible and can provide quantitative predictions of power draw, energy utilization, fracture and wear for screens, crushers and a broad range of mills. Previously, it has also demonstrated that two-dimensional modelling (of discs) is of almost no use since it cannot quantitatively capture the charge behaviour. Using spheres to model particles captures a great deal of the process in tumbling mills.

Detailed DEM analysis of AG and SAG mills has very clearly demonstrated that breakage in these devices is almost always the result of multiple collisions. Energy absorption by each size class of the charge is broadly proportional to the surface energy of the particles. Energy dissipation is predominantly from the shear components of collisions as particles mostly slide over each other rather than having head-on impacts. The energy spectra for the cement mill show that the use of finer feed strongly changes the way energy is consumed with sharp rises in the energy consumed by direct rock–rock collision and matching sharp reductions in rock–media and media–media collisions. Research into modes of breakage within these mills is continuing [29, 30, 33]. Adjusting operating conditions to reduce waste of energy (in collisions which cause only elastic particle loading) offers an important avenue for process development.

Liner wear evolution within AG/SAG mills can also be predicted with reasonable success using DEM. Modes of breakage and transport within stirred mills is now also an area of active research. The addition of realistic slurry behaviour via Smoothed Particle Hydrodynamics (SPH) offers substantial opportunities for the future as many aspects of wet comminution depend very strongly on transport behaviour—which is largely controlled by slurry flow.

Modelling of a grinding table has demonstrated that DEM when using a dynamic breakage model can predict reasonable particle flow patterns, fracture rates, resident and product sizes as well as help to understand the way in which the mill utilizes energy. The energy spectra obtained for the grinding table show important differences to the ball mill. Conversely, the overall energy absorption by each size class is shown also to be broadly dependent on the area of particles in each class.

Stirred mills use super-critical rotation speeds to generate high-particle pressures and high shear in order to increase the energy intensity of the grinding. A tower mill operates at speeds of around 6 times that of the comparable ball mill. This mill appears to be an effective design with good transport behaviour and with broad participation of the charge in the breakage. In particular, the energy dissipation rates are very uniform along the height of the mill.

The Isamill is a fully enclosed mill that operates at much higher speeds and when optimized for a particular ore can grind down to ultra-fine sizes. Here we have demonstrated the importance of including the fine feed ore in the model as it tends to isolate the media particles and ensures that the energy consumption is typically expended in contacts involving rocks with only limited media–media and media–liner collisions. The feed material is quite mobile and densely fills the interstices between the media particles starting from the mill shell. The distance that the feed reaching radially inwards therefore depends on the feed fill level. The energy dissipation is again dominated by the shear component. The normal energy spectra is shown to be bi-model with the first peak arising from the weaker rock–rock collisions and the higher energy second peak arising from the much stronger rock–media collisions. Finally, particle trajectories were used to explore the complex nature of the particle motion within the compartments between discs, spiralling axially between compartments and also flowing through the holes in the grinding discs.

DEM is increasingly useful as a tool that can help provide fundamental insights into comminution processes and into the behaviour of specific machines. It can contribute to design of new equipment, to improvement of existing equipment and to assist in increasing the operational efficiency of all comminution unit processes. Here we have used DEM to gain detailed insight into five different mills: SAG mill, a ball mill, a grinding table, a tower mill and an Isamill. Differences in the nature of their energy utilization can be deduced from their energy spectra and reveal both differences and similarities of operation.

ACKNOWLEDGEMENTS

The authors would like to acknowledge the contribution of Dave Morton to the modelling of the Isamill. The DEM tower mill modelling work reported in this paper has been partially funded by the Centre for Sustainable Resource Processing.

REFERENCES

1. Napier-Munn TJ, Morrell S, Morrison RD, Kojovic T. *Mineral Comminution Circuits*: *Their Operation and Optimization*. Julius Kruttschnitt Mineral Research Center: Indooroopilly, Qld., 1999. ISBN: 0 646 28861 X.
2. Mishra BK, Rajamani RJ. The discrete element method for the simulation of ball mills. *Applied Mathematical Modelling* 1992; **16**:598–604.
3. Mishra BK, Rajamani RK. Simulation of charge motion in ball mills. Part 1: experimental verifications. *International Journal of Mineral Processing* 1994; **40**:171–186.
4. Cleary PW. Predicting charge motion, power draw, segregation, wear and particle breakage in ball mills using discrete element methods. *Minerals Engineering* 1998; **11**:1061–1080.
5. Cleary PW. Charge behaviour and power consumption in ball mills: sensitivity to mill operating conditions, liner geometry and charge composition. *International Journal of Mineral Processing* 2001; **63**:79–114.
6. Cleary PW, Sawley ML. DEM modelling of industrial granular flows: 3D case studies and the effect of particle shape on hopper discharge. *Applied Mathematical Modelling* 2002; **26**:89–111.
7. Cleary PW. Axial transport in dry ball mills. *Applied Mathematical Modelling* 2006; **19**:1517–1527.
8. Rajamani RK, Mishra BK. Dynamics of ball and rock charge in sag mills. *Proceedings of the SAG 1996*, Department of Mining and Mineral Process Engineering, University of British Columbia, British Columbia, 1996.
9. Cleary PW. Modelling comminution devices using DEM. *International Journal for Numerical and Analytical Methods in Geomechanics* 2001; **25**:83–105.
10. Cleary PW. Recent advances in DEM modelling of tumbling mills. *Minerals Engineering* 2001; **14**:1295–1319.
11. Herbst JA, Nordell L. Optimization of the design of sag mill internals using high fidelity simulation. In *Proceedings of the SAG Conference*, Vancouver, BC, vol. IV, Barratt DJ, Allan MJ, Mular AL (eds). University of British Columbia: British Columbia, 2001; 150–164.
12. Morrison R, Cleary PW, Valery W. Comparing power and performance trends from DEM and JK modelling. *Proceedings of the SAG 2001*, vol. IV. University of British Columbia: British Columbia, 2001; 284.
13. Cleary PW, Hoyer D. Centrifugal mill charge motion and power draw: comparison of DEM predictions with experiment. *International Journal of Mineral Processing* 2000; **59**:131–148.
14. Cleary PW, Morrison R, Morrell S. Comparison of DEM and experiment for a scale model SAG mill. *International Journal of Mineral Processing* 2003; **68**:129–165.
15. Powell MS, McBride AT, Govender I. Application of DEM outputs to refining applied sag mill models. In *Proceedings*: *XXII International Mineral Processing Congress*, Lorenzen L, Bradshaw DJ (eds), Cape Town, South Africa, 2003; 307–316.
16. Hlungwani O, Rikhotso J, Dong H, Moyes MH. Further validation of DEM modelling of milling effects of liner profile and mill speed. *Minerals Engineering* 2003; **16**:993–998.
17. Bwalya MM, Moys MH. The use of DEM in predicting grinding rate. In *Proceedings*: *XXII International Mineral Processing Congress*, Lorenzen L, Bradshaw DJ (eds), Cape Town, South Africa, 2003; 1612–1617.
18. Haff PK, Werner BT. Computer simulation of the mechanical sorting of grains. *Powder Technology* 1986; **48**:239–245.

DOI: 10.1002/fld

19. Ristow GH. Granular dynamics: a review about recent molecular dynamics simulations. *Annual Reviews of Computational Physics* 1994; **1**:275–308.
20. Cleary PW. Discrete element modelling of industrial granular flow applications, TASK. *Quarterly—Scientific Bulletin* 1998; **2**:385–416.
21. Pöschel T, Buchholtz V. Complex flow of granular material in a rotating cylinder. *Chaos*, *Solitons and Fractals* 1995; **5**:1901–1912.
22. Potapov AV, Campbell CS. Computer simulation of Hopper flows. *Physics of Fluids* 1996; **8**:2884–2894.
23. Cleary PW. Large scale industrial DEM modelling. *Engineering Computations* 2004; **21**:169–204.
24. Campbell CS. Rapid granular flows. *Annual Review of Fluid Mechanics* 1990; **22**:57–92.
25. Barker GC. Computer simulations of granular materials. In *Granular Matter*: *An Interdisciplinary Approach*, Anita M (ed.). Springer: New York, NY, 1994.
26. Walton OR. Numerical simulation of inelastic frictional particle–particle interaction. In *Particulate Two-phase Flow*, Chapter 25, Roco MC (ed.). 1994; 884–911.
27. Schäfer J, Dippel S, Wolf DE. Force schemes in simulation of granular material. *Journal de Physique I* (*France*) 1996; **6**:5.
28. Williams JR, Pentland A. Super-quadrics and modal dynamics for discrete elements in interactive design. *International Journal of Computer-Aided Engineering—Engineering Computations* 1992; **9**:115–127.
29. Morrison R, Shi F, Whyte R. Modelling of incremental rock breakage by impact—for use in DEM models. *Minerals Engineering* 2007; **20**:303–309.
30. Djordjevic N, Morrison R, Loveday B, Cleary PW. Modelling comminution patterns within a pilot scale AG/SAG mill. *Minerals Engineering* 2006; **19**:1505–1516.
31. Sinnott MD, Cleary PW, Morrison RD. Analysis of stirred mill performance using DEM simulation. Part 1—media motion, energy consumption and collisional environment. *Minerals Engineering* 2006; **19**:1537–1550.
32. Cleary PW, Sinnott MD, Morrison RD. Analysis of stirred mill performance using DEM simulation. Part 2—coherent flow structures, liner stress and wear, mixing and transport. *Minerals Engineering* 2006; **19**:1551–1572.
33. Morrison R, Loveday B, Djordjevic N, Cleary PW, Owen P. Linking discrete element modeling to breakage in a pilot-scale AG/SAG mill. In *Advances in Comminution*, Kawatra SK (ed.). SME: Littleton, Colorado, 2006; 269–283.